

Article

Diurnal and Seasonal Variability of the Atmospheric Boundary-Layer Height in Marseille (France) for Mistral and Sea/Land Breeze Conditions

Aurélie Riandet ^{1,*}, Irène Xueref-Remy ¹, Ioana Popovici ^{2,3}, Ludovic Lelandais ¹, Alexandre Armengaud ⁴ and Philippe Goloub ³

- ¹ Institut Méditerranéen de Biodiversité et Ecologie Marine et Continentale (IMBE), Aix-Marseille Université, CNRS, Institut de Recherche pour le Développement (IRD), Avignon Université, 13290 Aix-en-Provence, France
² R&D Department, Cimel Electronique, 75011 Paris, France
³ UMR8518—LOA—Laboratoire d’Optique Atmosphérique, Centre National de la Recherche Scientifique (CNRS), University of Lille, 59000 Lille, France
⁴ AtmoSud, Regional Agency for Air Quality Monitoring, 13006 Marseille, France
* Correspondence: aurelie.riandet@imbe.fr

Abstract: Marseille (France) is a city on the Mediterranean coast characterized by two specific wind patterns: mistral (northwesterly wind blowing above 10 m/s) and sea/land breezes (southwesterly wind during daytime/northeasterly wind during the nighttime, blowing below 6 m/s). For the first time, this study investigates the diurnal and seasonal variability in the atmospheric boundary-layer height (ABLH) in Marseille for both wind patterns. A 532 nm aerosol lidar was installed in the urban center in the summer of 2021. The lidar installed in the winter of 2021–2022 had an additional near-infrared channel at 808 nm. The ABLH was extracted from the lidar datasets using a Haar wavelet method. For well-established mistral conditions, the ABLH reached to about 1000 m and showed a diurnal amplitude of ~650 m in winter and 740 m in summer, with a morning growth rate limited by turbulence. During sea breeze situations, the ABLH maxima were lower in both seasons (300–600 m) due to the sea’s thermal inertia. During land breeze situations, ABLH minima were estimated to be lower than 150 m. In summer, the Haar method was unable to calculate them because of unpronounced aerosol layers. While the near-infrared channel gives better results, the polarization of the green channel allows us to understand the type of aerosols and thus the origin of the air mass; a combination of the two gives complementary information.

Keywords: boundary-layer height; Marseille (France); aerosol lidar; coastal city



Citation: Riandet, A.; Xueref-Remy, I.; Popovici, I.; Lelandais, L.; Armengaud, A.; Goloub, P. Diurnal and Seasonal Variability of the Atmospheric Boundary-Layer Height in Marseille (France) for Mistral and Sea/Land Breeze Conditions. *Remote Sens.* **2023**, *15*, 1185. <https://doi.org/10.3390/rs15051185>

Academic Editor: Yaoming Ma

Received: 20 January 2023

Revised: 15 February 2023

Accepted: 18 February 2023

Published: 21 February 2023



Copyright: © 2023 by the authors. Licensee MDPI, Basel, Switzerland. This article is an open access article distributed under the terms and conditions of the Creative Commons Attribution (CC BY) license (<https://creativecommons.org/licenses/by/4.0/>).

1. Introduction

The boundary layer is defined as the layer of the atmosphere that is directly influenced by the Earth’s surface. Theoretically, after sunrise, the ground heats up, and, consequently, warms up the air masses that are in contact with it. As they become warmer, air masses also become lighter, and, thus, convective processes start and contribute to the increase in the atmospheric boundary-layer height (ABLH). During the nighttime, a temperature inversion settles, with a stable nocturnal layer in contact with the ground topped by a residual layer [1]. In this study, the ABL is defined as the mixed layer during the day (the lowest part of the atmosphere, which is unstable and characterized by convective mixing that develops during the morning) and the nocturnal boundary-layer height during nighttime. Thus, it represents the volume in which surface emissions are mixed in the lower atmosphere. In addition to having a diurnal cycle, the boundary layer is more developed during summer than winter due to more incoming solar radiation in summer, resulting in higher temperatures and stronger convective processes than in winter [2]. The ABLH also depends on the surface type. Indeed, due to the sea’s thermal inertia and its lower

roughness, compared with the land, which creates less turbulence, the ABLH over the sea is lower than over the ground and shows a less pronounced diurnal cycle [3,4]. The location of coastal cities at the interface of continental and marine influences makes them more difficult to study due to the different processes involved. Some studies of the variability in the ABLH in the Mediterranean basin have already been published. For example, [5] found a mean diurnal ABLH in Athens (Greece) of about 2000 m in July and about 1000 m in December. In Barcelona (Spain), [6] found ABLH values ranging from 300 to 1450 m over 3 years and depending on synoptic situations [7]. Elsewhere in continental Europe, [8] studied the ABLH over Hosvøre (Denmark) and found that the ABLH during summer was around 600 m, while it was around 650 m during winter.

The ABLH is a key parameter to characterize the variability in the boundary layer and is the main dilution factor of pollutant emissions. When the ABLH is well-developed, pollutants show relatively low atmospheric mixing ratios [9]. This has a direct impact on air quality. In fact, high-pollution events have been shown to be more likely associated with a shallower ABLH because pollutants are trapped and concentrated close to the ground [3,10]. Moreover, inferred ABLH datasets from field observations are needed to improve atmospheric transport models. Although progress has been made in the determination of the ABLH by atmospheric models during daytime and for well-mixed ABLHs [11], nocturnal and stable ABLHs and complex atmospheric situations remain challenging for most models [11].

The ABLH is not directly measured by instruments but can be inferred from other measurements. There are several ways to do this, but some of the most common methods use aerosol lidar measurements. The laser systems, which are used in this article, are based on particle scattering theory. They provide a continuous atmospheric aerosol profile in high temporal resolution (seconds to minutes), but need multiple data treatments and, thus, request a great investment. Moreover, the ABLH is challenging to infer from lidar measurements due to limitations in both methods and instruments [12–14].

Complex situations and/or environments and their effects on the ABLH are still poorly understood. Marseille, the second most populous city in France, is in the vicinity of the Mediterranean Sea. It is part of the SUD-Provence-Alpes-Côte-d’Azur (SUD-PACA) region, located in the south-east of France, extending from Camargue Park to the Italian border from west to east, and from Avignon and the Southern Alps to the sea from north to south. Marseille is located in the south of the SUD-PACA region in a coastal environment and is thus subject to both continental and coastal influence. Moreover, the SUD-PACA region is characterized by a complex topography that leads to two specific meteorological situations: the sea/land breeze and the mistral situations.

These two meteorological patterns were studied within the ESCOMPTE campaign, “Expérience sur Site pour COntraindre les Modèles de Pollution atmosphérique et de Transport d’Emissions” [15]. Within this campaign, which was carried out in the summer of 2001, the structure and daytime variability in the lowest altitudes of the atmosphere were investigated. The results of ESCOMPTE highlighted complex air circulation, including the interactions between hills and the sea in the bay of Marseille, as detailed below.

The mistral wind originates from synoptic north or north-west winds accelerated by constriction through the Rhône Valley, which separates the Massif Central from the Alps [16–18]. This process results in a cold wind from the north-west sector (between 290° and 360°), but with strong wind speeds above 16 m/s (official definition given by the French national meteorological service Météo-France, <https://www.meteofrance.fr/>, accessed on 5 January 2022). Once reaching Marseille, this cold wind is slowed due to the roughness of the city. Afterward, the mistral wind accelerates again over the sea due to the lower roughness of the marine surfaces compared to the continental surfaces. In the summer of 2001 during mistral situations, the ABLH was found to be relatively constant over Marseille in the daytime, at around 1000 m [17]. No results were published for nighttime or winter.

The alternation of sea/land breezes is a local process due to the proximity of Marseille to the Mediterranean Sea. During the day, the land surface warms up faster than the sea because of its proximity to the ground, and air circulation develops from the sea to the land; this phenomenon is called the sea breeze current. Sometimes, a reverse current in altitude can establish from the land to the sea [19]. After sunset, the land cools down faster than the sea, and the circulation in the opposite direction takes place, with a light wind blowing from the land to the sea: this is called the land breeze circulation. During the ESCOMPTE campaign, due to the special shape of the coastline in Marseille, two types of sea breeze occurred during the day: a local sea breeze perpendicular to the coastline, reaching up to a few kilometers inland, and a deeper sea breeze from the south, going up to 100 km inland [20]. In some cases, these sea breezes were observed to be “pulsed” by slope breezes on hills around Marseille and the SUD-PACA region [21,22]. Indeed, the marine air mass advected by the sea breeze is accelerated by slope breezes and, therefore, has less time to warm up. This reduces the sea–land temperature gradient between the sea and the land and, therefore, decelerates the sea breeze. In the city, the air mass warms due to higher heat fluxes, which contributes to the increase in the temperature gradient between the city and the sea [23] and, therefore, increases the speed of the sea breeze. This creates a pulsed sea breeze, making the daytime ABLH more discontinuous [20,24].

To our knowledge, there have been no studies carried out on the ABLH in Marseille in winter, or on its seasonal variability. Our paper is dedicated to partially filling this gap, presenting new results in both aspects to understand processes involved in the ABLH variability in a midlatitude coastal city. It presents the first measurements and results of ABLH variability in Marseille in winter and in summer since ESCOMPTE in 2001. The variability in the ABLH is studied on the diurnal and seasonal scales, focusing on typical sea/land breezes and mistral situations during the summer of 2021 and the winter of 2021–2022. Our ABLH datasets were obtained from lidar routine measurements in the city center of Marseille ($43^{\circ}18'18.94''N$; $5^{\circ}23'41.319''E$) using the Haar method [25]. We also dedicate a part of this paper to addressing the limitations of both methods and techniques, as this is a crucial point for the determination of the ABLH from the lidar data. In the first part of this paper, the ABLH datasets and methods used to obtain them are presented. Then, in the second part, the results of each case study per season are presented and discussed. Finally, the limitations of the instruments and methods are investigated, and some recommendations are made as to how to improve the ABLH calculations for this coastal city.

2. Materials and Methods

2.1. Instrumentation and Measurement Sites

The study site, called Marseille–Longchamp and abbreviated as LCP hereafter, belongs to the regional air quality agency ATMOSUD and Aix Marseille University (see Figure 1). It is located in the city center of Marseille ($43^{\circ}18'18.94''N$; $5^{\circ}23'41.319''E$). The site is located 2 km from the western coast and 10 km from the southern coast of the Mediterranean Sea (see Figure 1). In the North and the East, the city of Marseille is bordered by two hill massifs, respectively, the massif de l’Etoile (maximal height of 600 m) and the Sainte-Baume massif (maximal height of 800 m).

Lidar measurements presented in this study were collected in the summer of 2021 and the winter of 2021–2022 within the ANR COOL-AMmetropolis project. Table 1 describes the characteristics of the lidar instrumentation, depending on the measurement periods.

We installed a biaxial aerosol elastic CIMEL lidar CE376 (CIMEL, <https://www.cimel.fr/>, 2022, accessed on 15 December 2021) during the summer of 2021 and another in the winter of 2021–2022. Both were placed in a thermal enclosure to maintain the temperature of the instrument within the range recommended by the manufacturer. Both instruments can provide measurements from the altitude of the blind zone (see Table 1) to approximately 10,000 m above ground level (AGL) during nighttime and approximately 8000 m AGL during daytime. The lidar installed in summer 2021 takes measurements using a green laser

Nd:YAG with a wavelength of 532 nm, whereas the lidar installed for winter 2021–2022 uses two wavelengths, 532 nm (green laser Nd:YAG) and 808 nm (pulsed laser diode). The lidar datasets are corrected for the detector's deadtime, background, overlap, and range. The resulting signal is, hereafter, called the range-corrected signal (PR2) and is expressed in arbitrary units (a.u.). The different optical configurations between the green and near-infrared channels explain the difference in the altitude of the blind zone. The data quality check was performed by comparing the Rayleigh profile with the backscattering profile at aerosol-free altitudes to verify the functioning of the lidar.

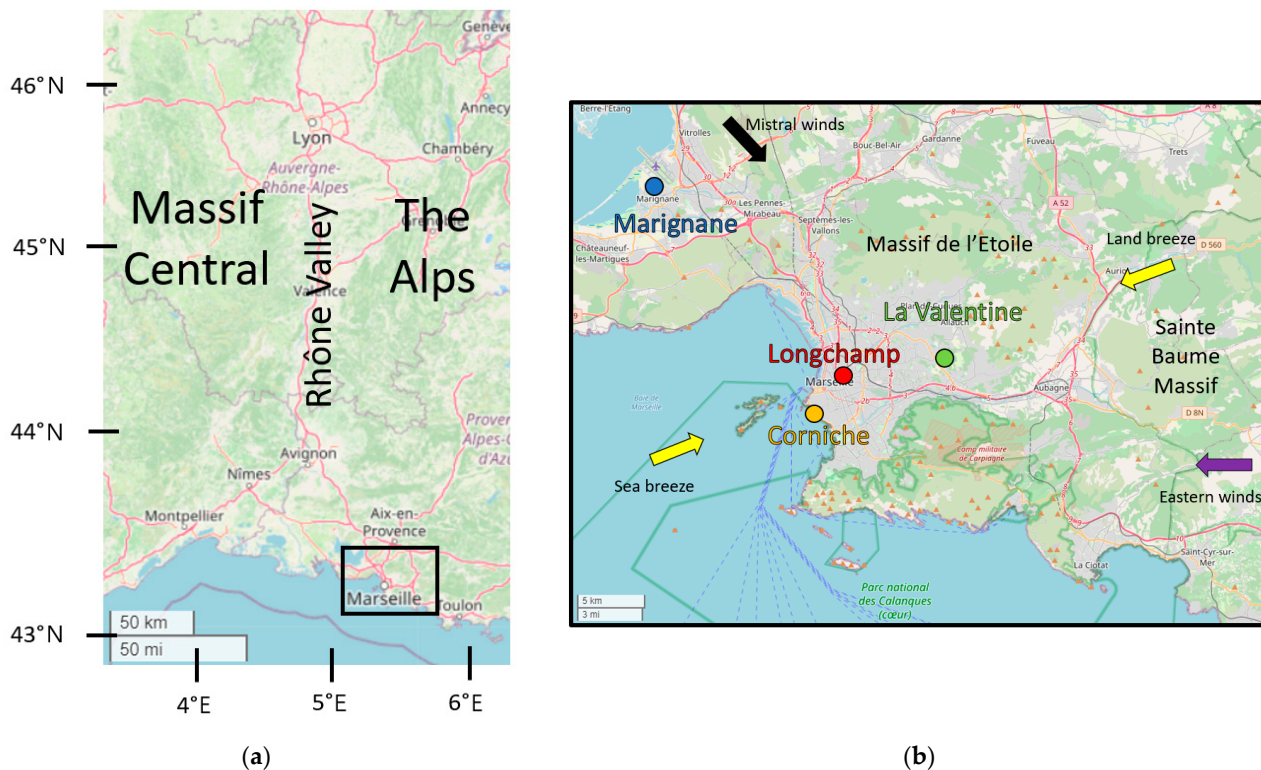


Figure 1. Map of the SUD–PACA region (left, (a)) and zoomed in on Marseille (right, (b)) showing the location of the measurement stations (blue: Marignane (AER), orange: Corniche (COR), red: Longchamp (LCP), green: La Valentine (LAV)). Arrows in yellow, black, and purple indicate the main wind regimes over the study periods, respectively, sea/land breezes (28%), mistral winds (21%), and eastern winds (17%).

Table 1. Technical characteristics of the CE376 lidars depending on the measurement periods in Marseille.

	Summer 2021	Winter 2021–2022
Lidar model	CE376-GP	CE376-GPN
Wavelength	532 nm	532 nm
Polarization	Parallel and perpendicular	Parallel and perpendicular
Period of measurement	16 July–14 September 2021	14 December 2021–28 February 2022
Range resolution Δz	15 m	15 m
Temporal resolution	1 min	1 min
Altitude of blind zone	100 m	250 m
Altitude of full overlap	1100 m	3000 m
		150 m
		1500 m

A sun–sky photometer CIMEL CE318 was also installed near the lidar on the roof of the station building, providing Angström exponents during the daytime.

As there were no meteorological data available on site, wind speeds, wind directions, and air temperature were acquired from surrounding stations located at Marseille airport

(AER), Corniche (COR), and La Valentine station (LAV). A summary of the meteorological data used is presented in Table 2.

Table 2. Meteorological instrumentation and parameters used.

	Marseille Airport Station (AER)	Corniche (COR)	La Valentine (LAV)
Coordinates	43°26'16"N 5°12'58"E	43°16'12"N 5°21'36"E	43°18'38"N 5°28'45"E
Height of the station (m ASL)	9	10	192
Meteorological parameters available		Temperature (°C) Wind speeds (°) Wind direction (m/s)	
Instrumentation	Temperature: OPALE station Wind speeds and directions: Alizia 312	Temperature/wind: Davis Instruments Vantage Pro 2	Temperature: MERCURY station Wind speeds and directions: Deolia 96
Time resolution (min)	60	30	60
Sampling height (m AGL)	Temperature: 1.5 Wind speeds and directions: 10	1.5	Temperature: 1.5 Wind speeds and directions: 10

AER and LAV stations belong to Météo-France (French national meteorological service), whereas COR belongs to the nonprofessional Static Infoclimat network (<https://www.infoclimat.fr/stations/static.php>, accessed on 8 August 2021).

2.2. Haar Method: Definition and Choice of Parameters

There are multiple ways to retrieve the ABLH from lidar backscattering aerosol profiles. One of the most widely used methods that have shown satisfactory results is the Haar method [14,26–31]. The Haar wavelet method, described by [25], is based on a BASIC algorithm developed by [32], written in Scilab language (<https://www.scilab.org/>, accessed on 14 February 2023) and dedicated to the analysis of lidar data, as follows:

$$h\left(\frac{z-b}{a}\right) = \begin{cases} +1 & \text{for } b - \frac{a}{2} \leq z \leq b \\ -1 & \text{for } b \leq z \leq b + \frac{a}{2} \\ 0 & \text{elsewhere} \end{cases} \quad (1)$$

where z is the altitude, b is the translation of the wavelet (m), and a is the dilation of the wavelet (m).

In this study, we used the detection of layers based on the convolution $W_f(a, b)$ of the lidar range-corrected signal $PR2(z)$ with an Haar wavelet:

$$W_f(a, b) = \frac{1}{a} \int_{z_{min}}^{z_{max}} PR2(z) h\left(\frac{z-b}{a}\right) dz \quad (2)$$

The maximum convolution of the Haar function W_f at altitude b is defined as the middle of the entrainment zone, which is chosen as the ABLH for this study (see Figure 2).

The Haar method depends on two parameters, the altitude range between the minimum altitude (z_{min} , m) and the maximum (z_{max} , m), within which the ABLH is searched, with dilation a .

To choose the best dilation, a , ideal profiles are selected for each period described hereafter. According to the literature, too high a dilation can lead to an overestimation of ABLH, whereas too low a dilation would not allow differentiation between noise and ABLH [27,33]. Visually, we excluded dilations that were too low and were unable to differentiate noise from the PR2 of the ABLH. We computed the ABLH for these ideal profiles with dilations ranging from $2\Delta z$ to $30\Delta z$, Δz being the vertical resolution of the lidar data, which are typical values found in the literature [25,32,33]. Then, we selected the dilation that most frequently selected the middle of the ABLH for ideal profiles, the latter being chosen when the ABL is very well mixed and the gradient between the free

troposphere and the ABLH is well marked. The dilation values used for this study are detailed in Section 4.3.

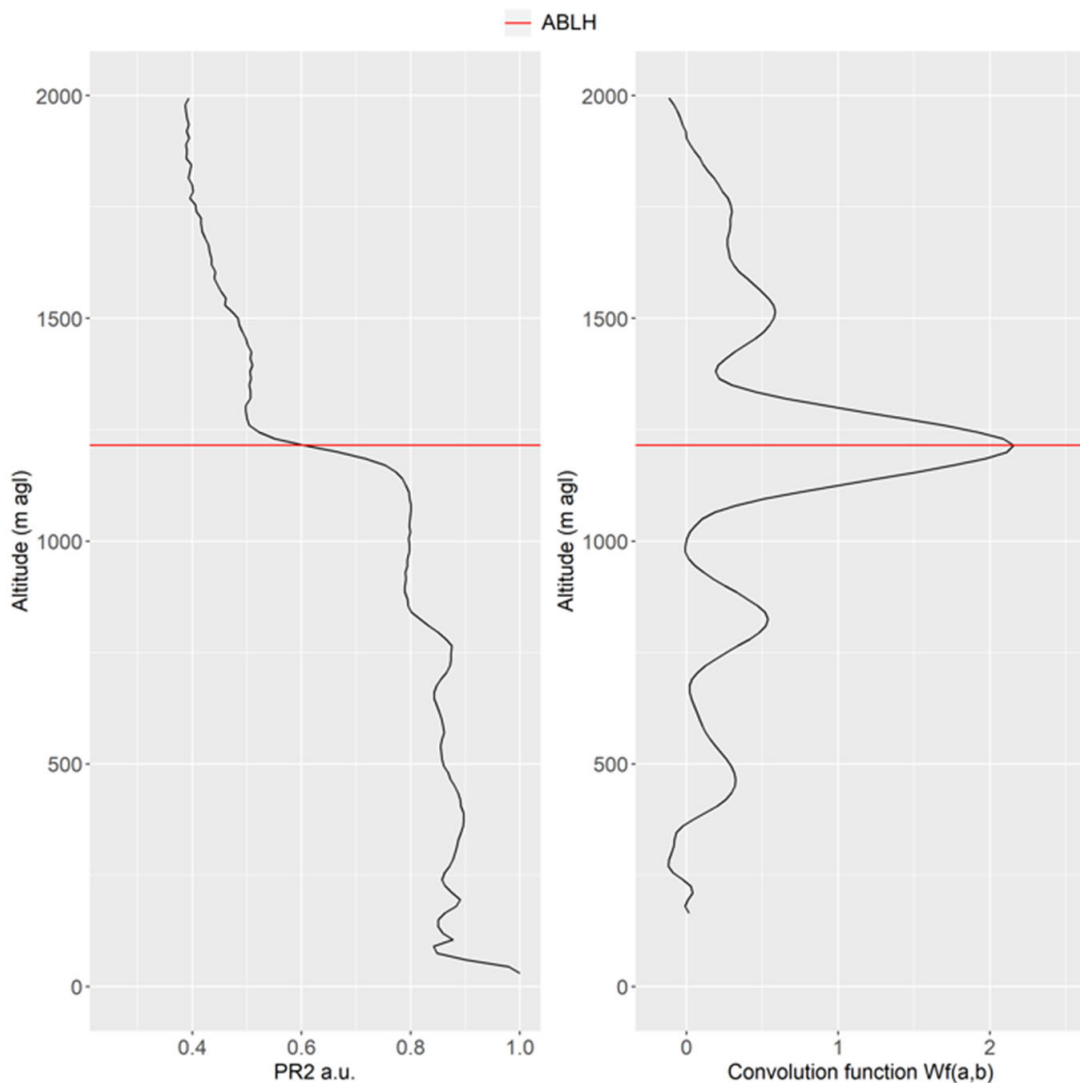


Figure 2. PR2 profile in arbitrary units (**left**) and convolution function $W_f(a,b)$ (**right**) for 18 August 2021 06:50. The ABLH is indicated by the red horizontal line and calculated as the b for which the $W_f(a,b)$ function is the maximum.

After computing the ABLH, the results are visually evaluated and attributed to four flags: “fog”, “good”, “bad”, and “undetermined”. The flag “fog” is set when there is dew on the lidar shooting window. The flag “good” is set when the computation of the ABLH gives good results according to the following criteria: (1) the aerosol layer detected by the algorithm shows a strong gradient in the profile, (2) over a period of 1 h, the ABLH detected by the algorithm is continuous and/or does not have a jump greater than 500 m (which is the maximum growth rate found in the literature), (3) the layer is in contact with the ground, and (4) the layer is overlaid by an aerosol-free layer. These criteria allow residual layers or unphysical jumps to be removed. The other data are flagged as “bad” when the algorithm detects an ABLH that clearly cannot be attributed to an ABLH. Finally, the “undetermined” flag is set for results that cannot be visually evaluated, that is to say, no clear boundary layer stands out. All statistics in this study are based on good data only, but “bad” and “undetermined” data will also be shown and discussed in Section 4.

2.3. Calculation of Depolarisation Ratio

Our lidar could separate the parallel and the perpendicular components of the linearly polarized green light emitted to the atmosphere and backscattered by atmospheric particles. The ratio between these two components gives information on the shape of these particles [34–37]. Each type of particle, depending on its emission process and source, has a characteristic shape and, therefore, a specific depolarization ratio. The depolarization ratio (δ or VDR) is calculated according to the following formula [36]:

$$\delta = \frac{\frac{\delta^*}{V^*} T_P - R_P}{R_S - \frac{\delta^*}{V^*} T_S} \quad (3)$$

where δ^* is the ratio between the parallel and perpendicular signals; T_P , T_S , $R_P = 1 - T_P$, and $R_S = 1 - T_S$ are the transmissions of the reflected (R) and transmitted (T) components on the Polarizing Beamsplitter Cube of the parallel (p) and perpendicular (s) light components; and V^* is the polarization calibration coefficient. Except for δ^* , R_P , and R_S , which were recalculated, all other parameters were given by the lidar manufacturer.

The δ value gives information about the sphericity of aerosols: low δ values are typical of spherical particles, whereas high δ values are found for nonspherical particles (see Table 3, [34–39]).

Table 3. Depolarization Ratio values for some aerosol categories at 532 nm.

Type of Aerosols	Summer 2021 Winter 2021–2022
Air molecules	0.0034
Clean marine	<0.04
Anthropogenic	0–0.15
Dust	0.25–0.31

As it is not easy to separate clean marine aerosols from anthropogenic aerosols, we also used the Angström exponent. This is defined as the ratio of the two AOD at λ_1 wavelength by AOD at λ_2 wavelength divided by the ratio of λ_1 by λ_2 from the photometer measurements. Here, we use the Angström exponent from 440–870 nm from AERONET products [40], which can help when discriminating anthropogenic aerosols from marine aerosols ([39]). Values above 1 are related to fine anthropogenic aerosols, while values below 1 can be associated with marine aerosols.

In Section 3, both VDR and Angström exponent are used as tools to determine the origin of air masses.

2.4. Models

In order to study the ABLH variability for different wind regime cases and seasons, the reanalysis from weather forecast model outputs was used. They are available on the website www.meteociel.fr. For the description of the synoptic situations over Europe (in Section 2.5), the chosen model was ECMWF ERA5 reanalysis, with a spatial resolution of 30×30 km, and performed four times per day at 00:00 UTC, 06:00 UCT, 12:00 UTC, and 18:00 UTC with sea-level pressure and 10 m wind speed and direction fields.

The sea temperature was taken from Medspiration SST (<https://cersat.ifremer.fr/Projects/Previous-projects/Medspiration>, accessed on 9 January 2023) satellite data.

2.5. Description of Meteorological Conditions

Table 4 lists the dates, wind regimes, and seasons of the four events studied below. A short name is associated with each event.

Table 4. Short name, season, wind regime, and period for each of the four studied events.

Abbreviation	Events	Dates (UTC)
SM	Summer 2021 mistral	16 August 2021 00:00–19 August 2021 04:00
WM	Winter 2021–2022 mistral	18 February 2022 22:00–23 February 2022 23:59
SB	Summer 2021 sea/land breezes	4 September 2021 00:00–6 September 2021 23:59
WB	Winter 2021–2022 Sea/land breezes	14 December 2021 00:00–17 December 2021 23:59

In this study, all hours and dates are given in UTC. Altitudes are defined as meters above ground level (AGL).

Mistral situations took place from 16 August to 19 August 2021 for SM and from 19 February to 23 February 2022 for WM. Sea/land breeze situations took place from 4 September to 6 September 2021 for SB and from 14 December to 17 December 2021 for WB.

For SM, a high-pressure area was located over the Atlantic Ocean whereas a relatively low-pressure area was located over the Gulf of Genoa. During the WM, the high-pressure area was located over the Azores islands and extended over France by a ridge (see Figures 3 and 4).

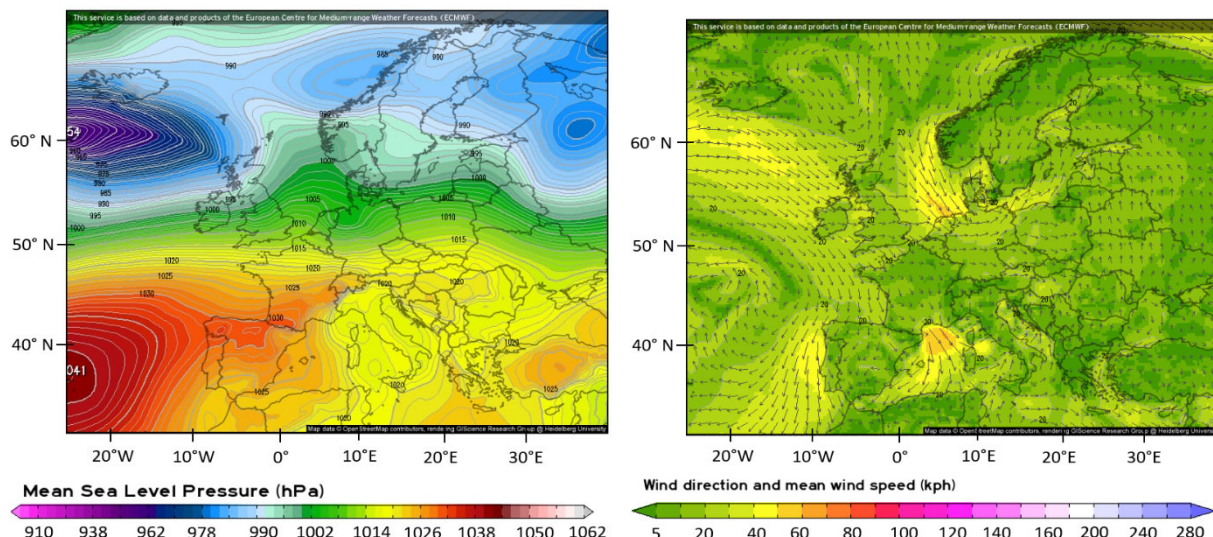


Figure 3. Sea-level pressure (left) and 10 m wind directions and speeds by ECMWF reanalysis for 17 August 2021. On the left, colors indicate the mean sea-level pressure and lines highlight the isobars. On the right, arrows indicate the wind direction and the colors indicate the wind speeds. Source: (meteorologix.com), accessed on 8 February 2023).

Both situations resulted in a northerly wind over France and a north/north-westerly synoptic wind (large-scale wind related to pressure conditions) over France. In the southeast of France, these winds were accelerated by a constriction in the Rhône Valley and resulted in relatively high wind speeds from the northwest in Marseille. Over the Mediterranean Sea, the wind merged with the Tramontane winds (north-easterly wind blowing between the Pyrenees and the Massif Central) and, because of the lower roughness of the sea compared to the continental ground, the resulting wind was accelerated. That is why COR (which is the closest station to the sea) showed higher wind speeds than LAV and AER. Wind directions during mistral situations were very constant over time ($315 \pm 1^\circ$ and $308 \pm 0^\circ$

for SM and WM, respectively, at AER), with high wind speeds during the whole periods (10.1 ± 3.8 m/s and 8.9 ± 4.1 m/s).

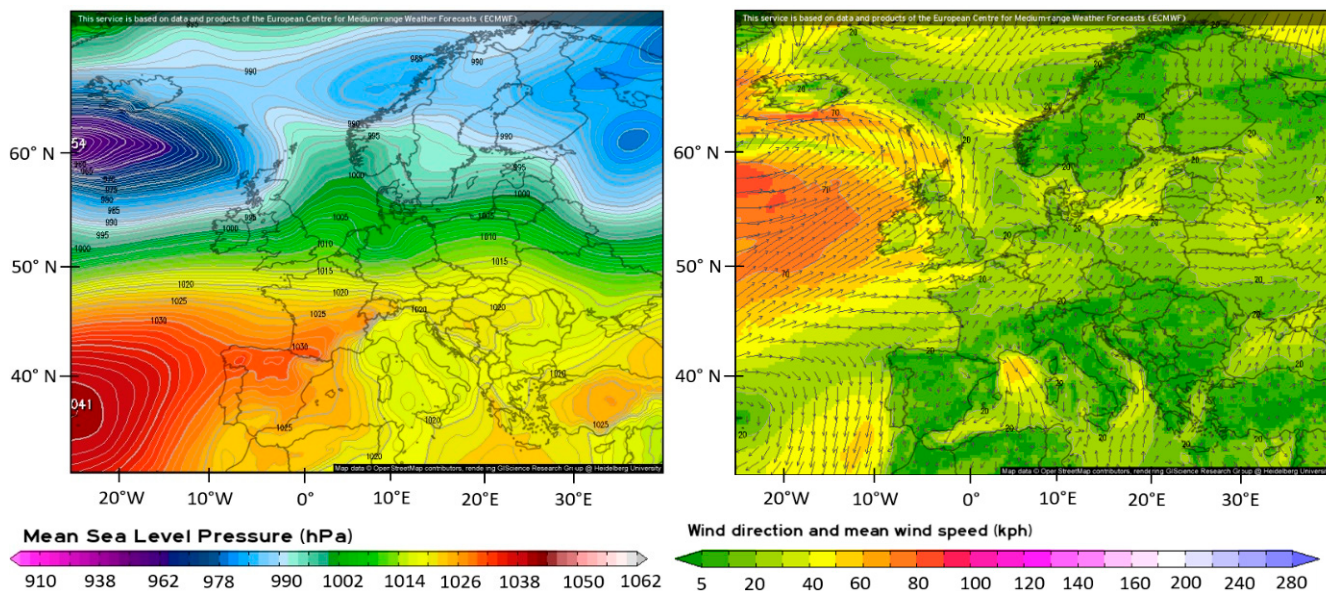


Figure 4. Sea-level pressure (left) and 10 m wind directions and speeds by ECMWF reanalysis for 20 February 2022. On the left, colors indicate the mean sea-level pressure and lines highlight the isobars. On the right, arrows indicate the wind direction and the colors indicate the wind speeds. Source: ([meteorologix.com](https://www.meteorologix.com)), accessed on 8 February 2023).

Controversially, synoptic situations for sea/land breeze situations during summer and winter were associated with high-pressure areas over Europe. This resulted in the absence of synoptic winds over the southeast of France, which favored the installation of the sea/land breeze situations (see Figures 5 and 6).

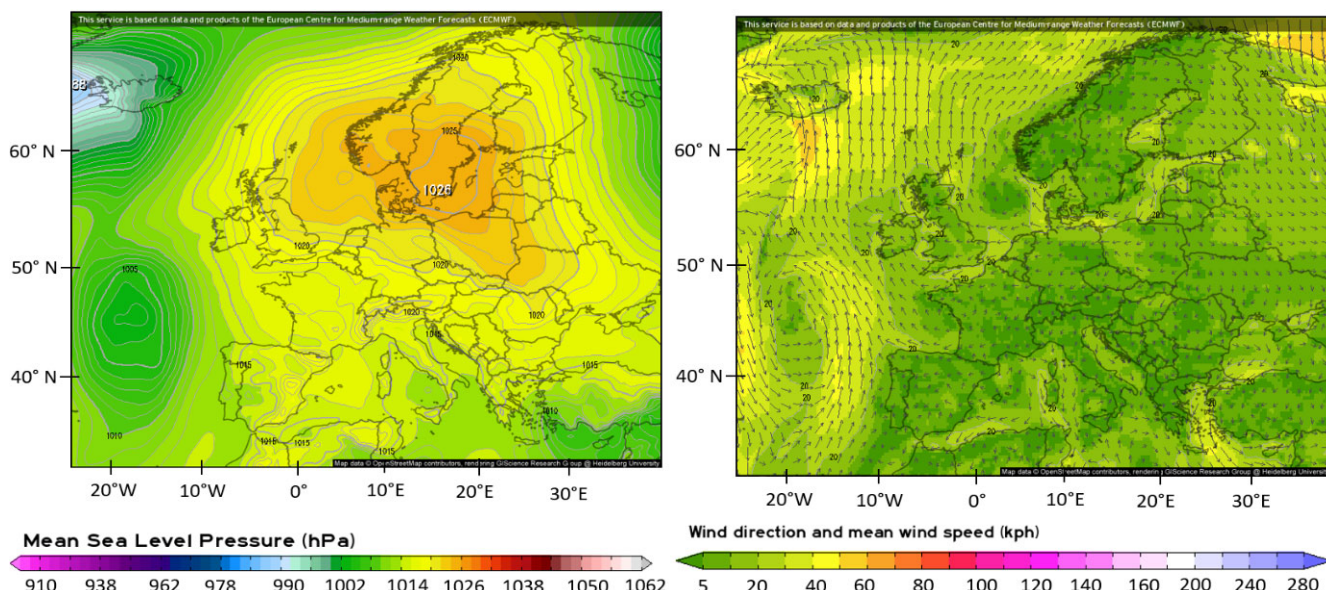


Figure 5. Sea-level pressure (left) and 10 m wind directions and speeds by ECMWF reanalysis for 5 September 2021. On the left, colors indicate the mean sea-level pressure and lines highlight the isobars. On the right, arrows indicate the wind direction and the colors indicate the wind speeds. Source: ([meteorologix.com](https://www.meteorologix.com)), accessed on 8 February 2023).

Sea/land breeze situations are established because there is a difference in temperature between the sea and the land. During SB, sea surface temperatures were around 23.0 °C and 15.0 °C for SB and WB, respectively, whereas, the temperature maxima over the continent at LAV were 27.9 °C and 16.8 °C for SB and WB, respectively. During SB, land breezes occurred during nighttime, blowing from the northeast sector with relatively low wind speed values below 2 m/s. The land and the sea breezes had the same direction during summer; however, the sea breezes lasted shorter than the land breezes.

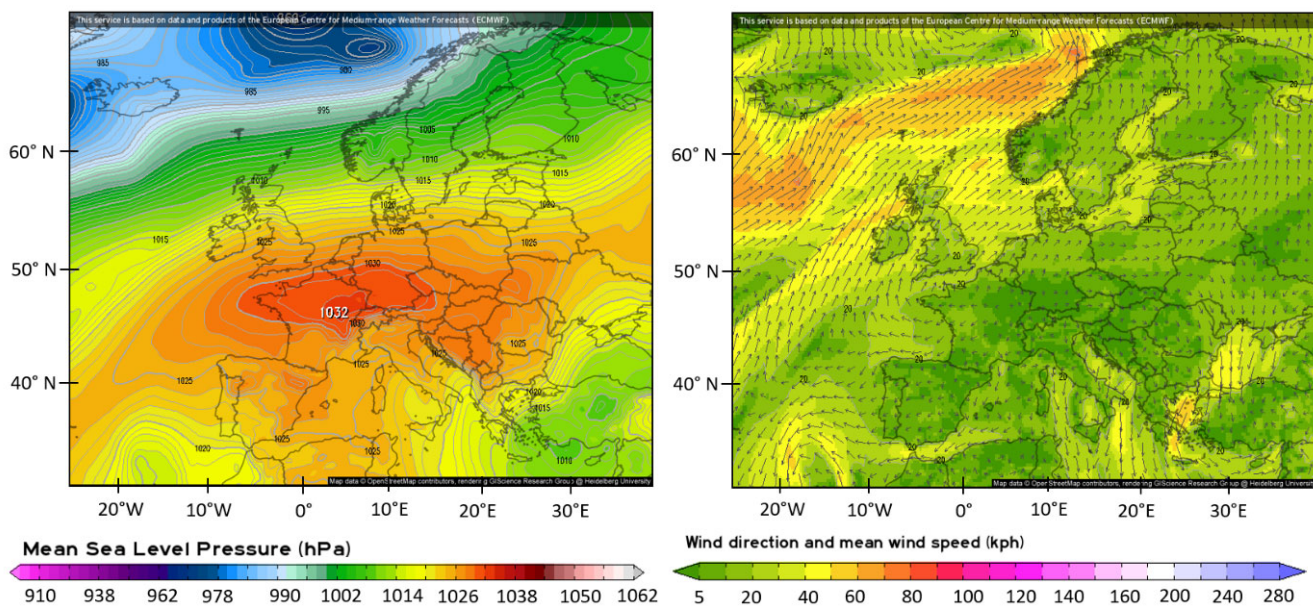


Figure 6. Sea-level pressure (left) and 10 m wind directions and speeds by ECMWF reanalysis for 15 December 2021. On the left, colors indicate the mean sea-level pressure and lines highlight the isobars. On the right, arrows indicate the wind direction and the colors indicate the wind speeds. Source: (meteorologix.com, accessed on 8 February 2023).

3. Results and Discussion

3.1. Overview of the ABLH Timeseries and the PR2 Quicklooks

The time series of the ABLH over Marseille for the four periods defined in Table 4 are presented in Figure 7 for the green channel. The colored quicklook displayed on top of the ABLH time series represents the PR2 as a function of time and altitude.

As shown in Figure 7, the allocation of data in flags is different from one event to another. “Fog” data represent 7%, 0%, 3%, and 0% for SM, WM, WB, and SB, respectively. “Good” data represent 65%, 73%, 51%, and 26% for SM, WM, SB, and WB, respectively. “Bad” data represent 1%, 24%, 16%, and 32% for SM, WM, SB, and WB. Finally, “Undetermined” data represent 27%, 3%, 30%, and 42% for SM, WM, SB, and WB, respectively.

The “good” data represent more than half of all the data in all of the events, except for SB, where a complex stratification explains the lower percentage of “good” data (as discussed in Section 4).

Apart from SM, for which this flag was only assigned to a low amount of data, the “bad” flag was mainly found during the day on 20 February and 21 February in the course of WM. During SB, the “bad” flag was mainly found during nighttime on 5 September, where topped boundary-layer clouds were detected by the algorithm and thus, no ABLH was calculated. During WB, the “bad” flag was found during nighttime: (1) when there was no observed aerosol (e.g., from 15 December 00:00 and 15 December 11:00 and from 11 December to 16 December 10:30; (2) when the algorithm wrongly detected the ABLH (from 15 December 19:00 to 16 December 09:00). In the latter situation, the ABLH clearly decreased on 15 December 19:00 (as observed in Figure 8 below), which likely signified that

the ABLH was below the minimum detection altitude of the lidar and, thus, lower than 150 m.

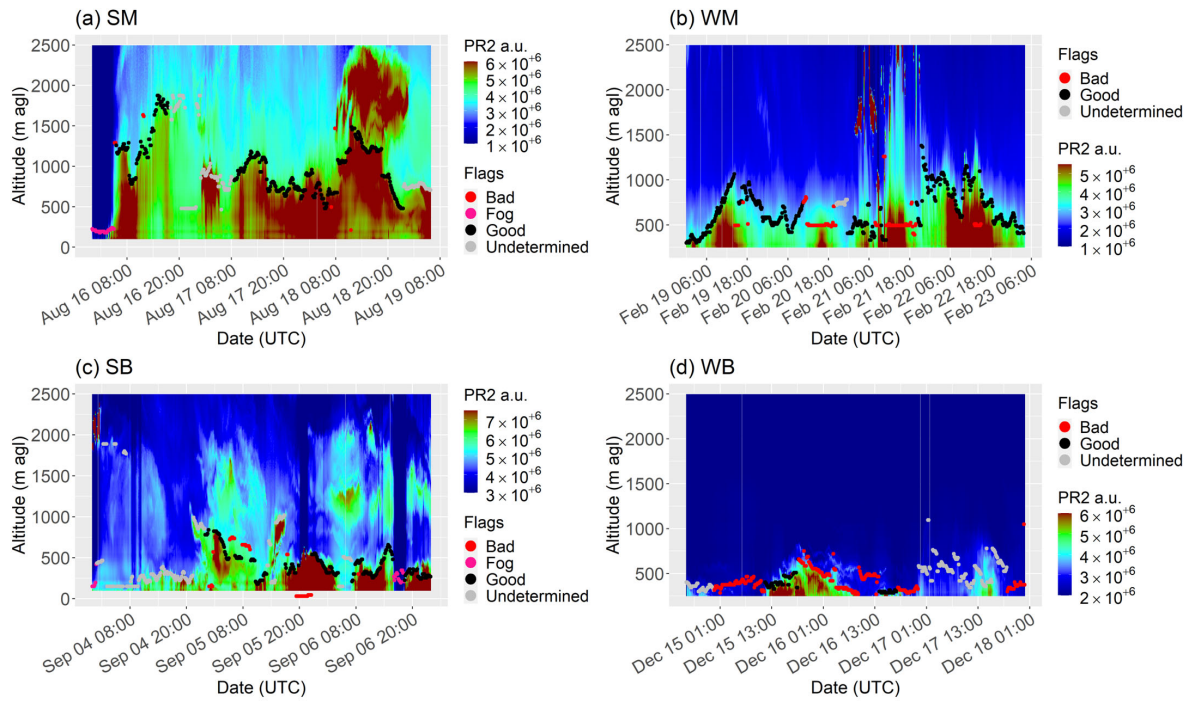


Figure 7. Time series of the green channel PR2 for the SM event (a), the WM event (b), the SB event (c), and the WB event (d). Color dots represent the ABLH (pink, black, red, and gray stand for fog, good, bad, and undetermined flags, respectively).

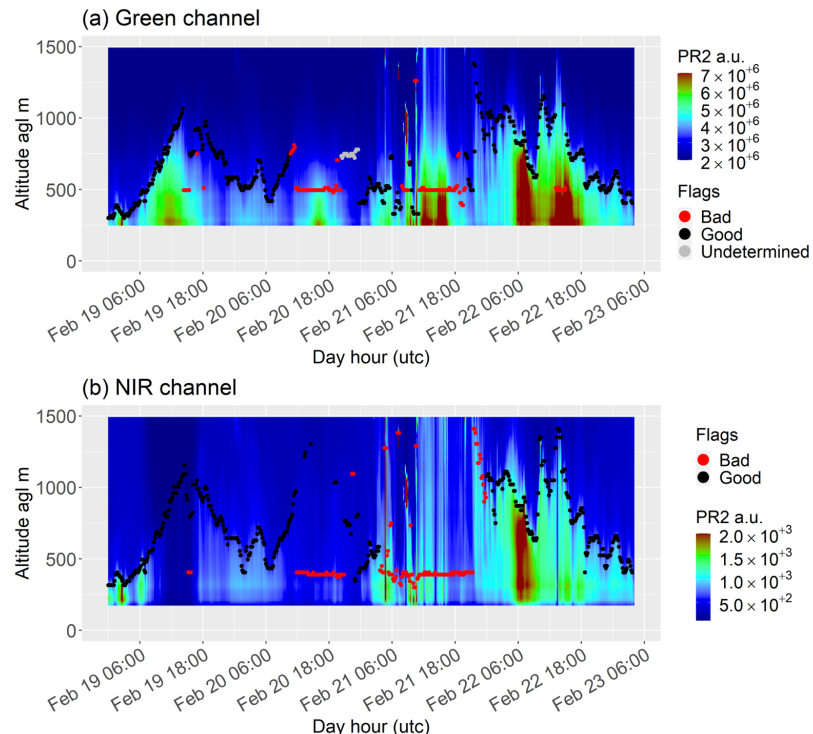


Figure 8. Time series of the PR2 signals inferred from both the green (a) and the near-infrared (NIR, b) channels during the WM event. The black dots represent the ABLH applying the Haar wavelet method on the green and near-infrared datasets.

Finally, the “undetermined” flag occurred during SM from 16 August 18:00 to 17 August 08:30, when the aerosol gradient defining the top of the ABL was unpronounced or there were multiple aerosol layers with similar gradient values which both prevented the algorithm from detecting the ABLH. The same conclusions were drawn for WM. The complex stratification occurring during that event also prevented the algorithm from detecting the ABLH and, thus, increased the number of “undetermined” cases. Finally, this flag was mainly attributed to data ranging from 17 December 00:00 to 17 December 19:40, where there was a relatively low aerosol content during nighttime (which prevented us from determining whether this layer was a residual layer or the ABLH) and during the daytime (where a complex stratification was observed).

The near-infrared channel can bring additional information.

During WM, the main differences between the green and the near-infrared channels were found on 20 December, when the algorithm totally failed to detect the ABLH inferred from the green channel, whereas it satisfactorily detected the ABLH inferred from the near-infrared channel (see Figures 8 and 9). The algorithm behaved similarly regarding the detection of the ABLH maximum on 22 December.

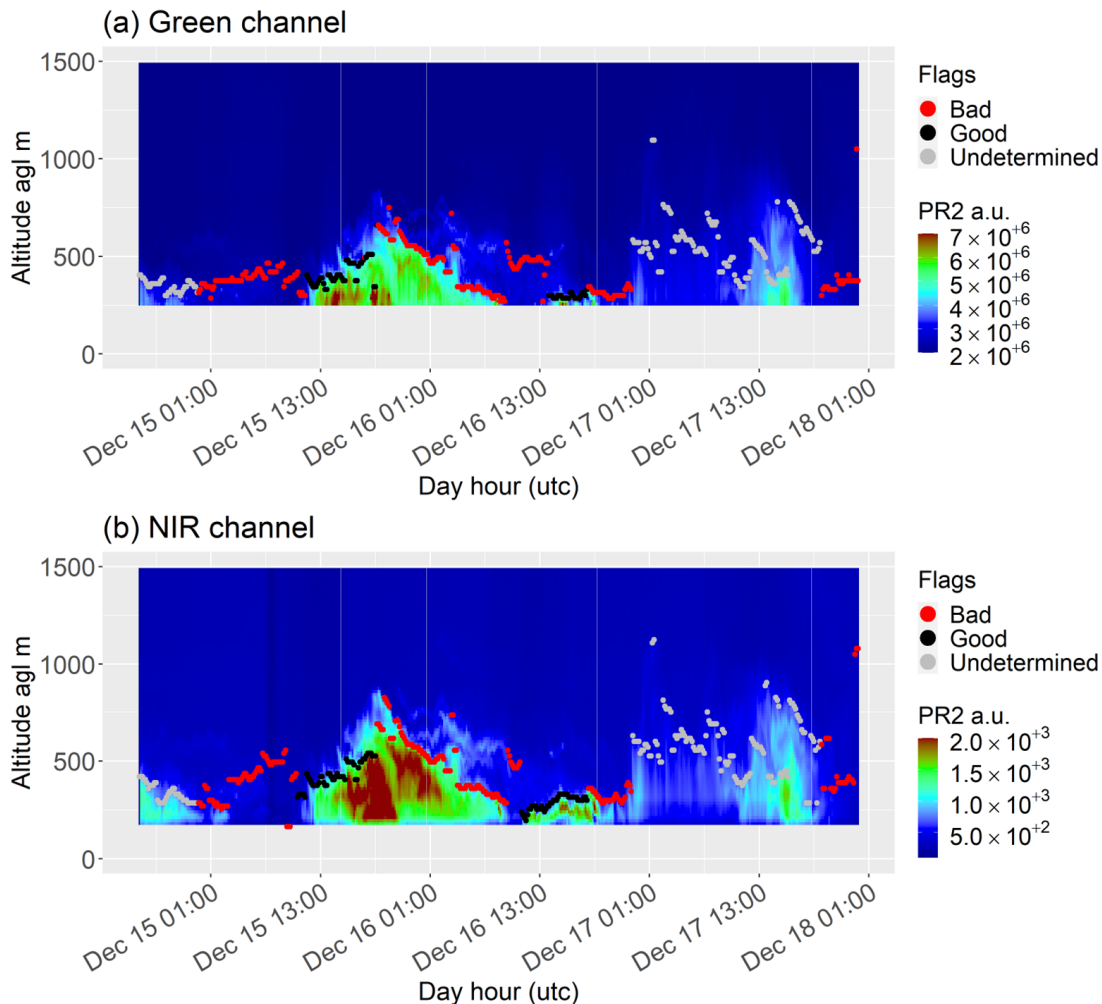


Figure 9. Time series of the PR2 signals inferred from both the green (**a**) and the near-infrared channels (NIR, **b**) during the WB event. The black dots represent the ABLH applying the Haar wavelet method on the green and near-infrared datasets.

During WB, there was no difference between the ABLH inferred from the green and the near-infrared channels, except on 16 December. For that day, the ABLH was seen earlier in the near-infrared channel (from 10:30 with the near-infrared channel compared to 11:30

with the green channel): when the ABLH grew, it first exceeded the blind zone of the near-infrared signal (150 m) and then the blind zone of the green signal (250 m).

Unfortunately, there was no near-infrared observation during the summer of 2021. In the winter of 2021–2022, the mean differences between the estimated ABLH values were small from both channels, with a mean difference of -31 ± 18 m for SB and -37 ± 177 m for WM for “good” data (which represented less than 10% of the ABLH values). This is why, in the following, we will mostly present the ABLH values from the green channel. The ABLH values inferred from the near-infrared channel are followed by a “**” if they provide additional information compared to the ABLH values from the green channel.

3.2. Diurnal Cycle, Characteristics, and Seasonal Variability

In this section, we attempt to infer the diurnal cycle of the ABLH for the four events.

For SM, as there was fog in the morning and no strong aerosol gradient in the evening of 16 August, it was impossible to assess information on the ABLH minimum on 16 August and 17 August. For WM, in the following, only the 19 February, 21 February, and 22 February datasets were retained for calculating the ABLH diurnal cycle as there was no “good” data available on 21 February. For SB, only the nighttime of 5 September to 6 September and the day of 6 September were considered for the study of the diurnal cycle because they were the single periods when the ABLH was calculated correctly. Finally, for WB, 2 days (15 December and 16 December) and three night times (14 December–15 December, 15 December–16 December, and 16 December–17 December) were considered. For each day, the ABLH growth rate was calculated from the period between the ABLH daily minimum and its maximum.

The mean value of the ABLH was higher during summer than during winter for both mistral situations (995 ± 323 m versus 659 ± 225 m, respectively), and sea/land breeze situations (402 ± 159 m versus 350 ± 51 m, respectively). This seasonal variability comes from the insolation difference between summer and winter, which results in more pronounced convective mixing in summer than in winter and, thus, a more developed ABLH. Note that the standard deviation was lower during sea/land breeze situations as (1) there was less “good” data in these situations, and (2) the amplitude of sea/land breeze situations was lower than that of the mistral situations (see below, where the amplitude is discussed). The standard deviation was particularly low during WB as “good” data only occurred during the daytime.

Sea/land breeze situations exposed the observation site to marine air masses. This leads to 1) less seasonal variations in the ABLH due to the large thermal inertia of the sea, 2) less turbulence because of a lower roughness of the sea surface compared to the ground surface, and 3) lower air temperatures, thus lower convective development associated with these events. Moreover, mistral winds are associated with strong winds bringing more mechanical turbulence. The roughness of the city may also play a role in increasing the turbulence over the city, as has already been shown in [41]. However, we do not have enough measurements or small-scale models to fully investigate the origin of the turbulence. This can explain why the sea/land breeze situations were associated with lower mean ABLHs than the mistral situations.

Several differences in the ABLH diurnal cycles during sea and/or land breezes were observed between both seasons, but differently for mistral situations. During winter, the ABLH associated with the land breeze was lower than the ABLH associated with the sea breeze, whereas it was the opposite during summer. This can be explained by the thermal inertia of the Mediterranean Sea, the latter being warmer (colder) than the land during winter (summer).

The diurnal amplitude of the ABLH ranges from 745 m to 1090 m and from 645 m to 900 m for SM and WM, respectively, with maximal values during daytime and minimal values during nighttime following the diurnal temperature variations. Diurnal amplitudes are thus similar between summer and winter for mistral situations, whereas the amplitude of temperature is higher in summer than in winter. As the ABLH during mistral is partly

driven by mechanical turbulence, the diurnal cycle is thus less sensitive to seasonal temperature variations than the ABLH during sea/land breeze situations. However, the existence of a diurnal cycle with higher values during daytime than nighttime means that there is also an impact of thermal processes on the ABLH diurnal variability.

During SB, due to “bad” and “undetermined” flagged data, it was impossible to give a precise diurnal amplitude of the ABLH. In the case of WB, the diurnal amplitude of the ABLH ranged from 180 m to 450 m, which is twice lower than the mistral situations. The amplitude of the air temperature was higher in summer than in winter for both mistral and breeze situations (mean temperature amplitude of 8.5 °C for SM, 6.6 °C for WM, and 11.5 °C for WB) because of the difference in time of insolation and solar heating intensity between summer and winter. However, it is noticeable that the diurnal amplitude of the ABLH was higher for mistral situations when the amplitude of the air temperature was lower than for sea/land breeze situations. During the nighttime, radiative cooling induces a substantial cooling of the air mass (from 0 °C to 5° C in winter), which requires more energy to start the convective mixing than in mistral situations. Thus, even if the air temperature increase is faster than in a mistral situation, the amplitude of the ABLH is lower in sea breeze than in mistral.

This process also explains the difference in the ABLH maximum value between mistral and sea/land breeze situations: this maximum is higher in mistral situations than in sea breeze situations (1200–1860 m for SM, 1200–1380 m for WM, 660 m for SB, and 330–450 m for WB). Furthermore, in breeze situations, the ABLH maximum showed a small seasonality as the range of maximum ABLH for the SB situation included the maximum of the ABLH inferred for WM situations, even if there is a significant temperature difference between both seasons (23 ± 4 °C for SM and 12 ± 2 °C for WM). This is due to sea thermal inertia, which induces a shallow ABL. Mistral is characterized by higher wind speeds than average (5.3 ± 4.2 m/s for summer 2021; 4.2 ± 4.0 m/s for winter 2021–2022), and atmospheric mechanical turbulence is increased, which does not depend on the season: which explains that there was almost no difference between the maximum for SM and WM. During the SB, the ABLH showed two maxima. This might be explained by the establishment of the sea breeze and the passage of the sea breeze head. Indeed, this maximum ABLH lasted approximately 1 h and was correlated with an increase in wind speed observed at the COR station, as well as a wind direction rotation observed at all of our meteorological stations. This sea breeze head is sometimes associated with high turbulence, which can increase the ABLH [21]. Once this sea breeze head passes, the ABLH decreases suddenly, leaving room for the shallow marine boundary layer. During the day, the sea breeze speed increases with the increase in temperature as the contrast between ground temperature and sea temperature increases. The air mass passes over Marseille, it does not have enough time to stay over the ground and to warm up, leading to a slight decrease in the ABLH [42]. Once the air temperature maximum is reached (at 12:00), the wind speed decreases, allowing the ABLH increases to reach a maximum at 15:00. One explanation for that increase could be that, with the decrease in the wind, as the ground is still warm the ABLH develops.

The ABLH growth rates in mistral situations were quite variable and ranged from 62 m/h to 461 m/h, while for sea/land breeze situations it was much less variable, ranging from 11 m/h to 123 m/h. Except for 22 February, there was no seasonality in the growth rate of mistral situations. The growth rate on 22 February was particularly high compared to other values of the event (461 m/h), but we lack the information to understand this phenomenon. For sea/land breeze situations, we infer higher ABLH growth rate values in summer than in winter; however, the lack of data below 150 m leads us to be cautious about the conclusions and their significance.

Some phenomena occurred both during summer and winter, in particular in mistral situations. When the ground heats the air mass just above it, it should normally trigger the convection process, leading to the development of the ABLH. However, in our case, the air was mixed by the strong mechanical turbulence induced by the mistral wind [17]. Thus, it took more time for the ABLH to develop compared to theoretical non-mistral

situations. This was characterized by the lowest air temperature amplitude during SM and WM situations ($7.1\text{ }^{\circ}\text{C}$ and $6.1\text{ }^{\circ}\text{C}$, respectively). The same process also happened in the evening during ground cooling, when a temperature inversion could theoretically occur due to the cooling of lower air masses in contact with the ground. If cooling has a stronger impact than turbulence, we would observe (1) the decoupling of the mixed layer into a night layer and a residual layer, which was only observed at the end of the night in our case, (2) a temperature amplitude close to the average amplitude of the season ($8.2\text{ }^{\circ}\text{C}$ for the summer of 2021 and $10.1\text{ }^{\circ}\text{C}$ for the winter of 2021–2022), whereas we observed a lower air temperature amplitude ($7.1\text{ }^{\circ}\text{C}$ and $6.1\text{ }^{\circ}\text{C}$ for SM and WM, respectively). Moreover, we also observed a lower rate of temperature decrease in the evening than the season's average. All of these elements allow us to conclude that the high wind speeds mixed the air mass, limited the cooling, and prevented the formation of a temperature inversion. This was only observable when the mistral is constant and established. When the mistral wind slows down (below 10 m/s), the ABL is no longer well mixed and the thermal effects take precedence over dynamic processes. Moreover, wind directions are no longer constant from the northwest, but vary from site to site during the day. Mistral winds no longer take over the local circulations, which are established during the day [43].

3.3. Aerosol Layer Composition and Dynamics

In WM, we noticed very low values below 0.02, typical of marine and/or anthropogenic aerosols, and relatively high VDR values, typical of continental aerosols [34,35,44,45], see Figure 10.

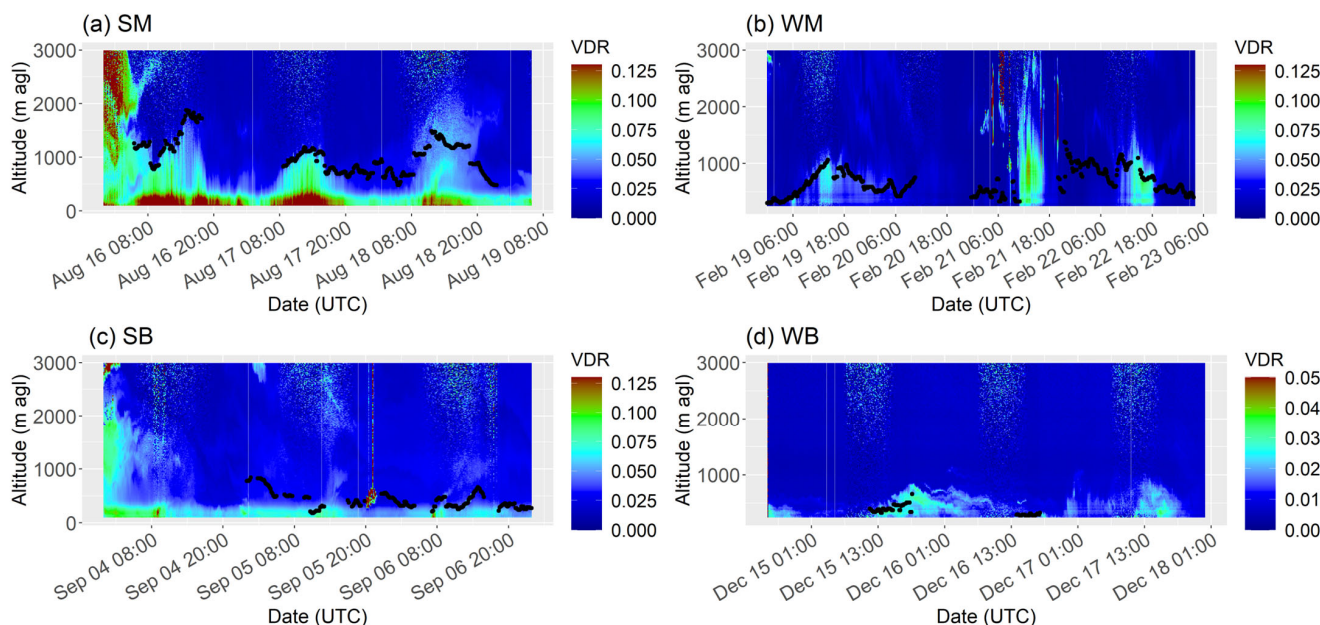


Figure 10. Depolarization Ratio (VDR) during SM event (a), WM event (b), SB event (c), and WB event (d); black dots stand for the ABLH calculated and then visually flagged as “good”. Note that the VDR scale is adapted to each case.

It was expected that the observed aerosols were of continental origin; but in our case, the very low VDR values were associated with relatively low Angström exponents, reflecting more marine aerosols. However, looking at the LAV wind direction station, we could note that relatively low VDR values were associated with west-northwest winds and an increase in temperature, which could be explained by the reinforcement of westerly flow passing over the Mediterranean Sea and loaded in marine aerosols. For SM, only anthropogenic aerosols (VDR of $0.10\text{--}0.15$ and an Angström exponent higher than 1.00) were observed, which indicates the nonmarine and, thus, the continental origin of the air mass.

In both sea/land breeze cases, the presence of anthropogenic aerosols was observed in the ABLH mainly. They come from pollution sources rather than clean marine aerosols. However, the stratification of aerosol layers in the first few kilometers of the atmosphere is quite different during summer and winter. Indeed, summer shows aerosol layers up to 4000 m, whereas in winter there is no aerosol layer above the boundary layer. Possible explanations are the following: (1) in summer, synoptic conditions are more often anticyclonic, pushing forward the stagnation of aerosols, whereas in winter there are frequent passages of low-pressure areas and fronts which promote the aerosol dispersion; (2) summer sea breezes are stronger and go further inland than winter ones, developing more into sea breeze cells, whereas in winter, breezes are weaker and land/sea temperature differences are less pronounced, limiting the development of sea breeze cells.

3.4. Comparison with the Literature

3.4.1. Mistral

In summer, the ABLH for mistral situations exhibited day-to-day variability. One possible explanation of the ABLH's highest values encountered during such situations would be an interaction with the French Prealps. In [46], the three possible main patterns downwind of the mistral flow are highlighted: mountain waves, wave breakings, and flow splitting. More data about the dynamics of the ABLH upstream of the site as well as modeling studies would allow us to identify the role of these different patterns. Another explanation for these very high values could be the existence of a hydraulic jump associated with the mistral regime [17,47].

Whereas in both situations, winds have a continental origin, the ABLH growth rate on 17 August was very low compared to the literature for Paris in France [48] during summer. This reinforces the hypothesis that an established and constant mistral wind diminishes the development and the decrease in the ABLH, as the ABLH development in Paris is mainly explained by thermal processes, whereas in Marseille, during mistral situations, high wind speeds lead to high mechanical turbulence. The ABLH on 17 August coincides very well with what the authors of [17] found, with an ABLH around 1000 m during summer constant during the day and relatively low compared to what has been observed at continental sites [27]. The amplitude of the ABLH diurnal cycle was found to be in the minimum values of the range of values found in the literature [49,50], which can be explained both by a smaller growth and a smaller decrease in the ABLH.

On 18 August, mistral wind speeds were quite low (below 10 m/s). The ABLH amplitude on that day was found to be around 1100 m, which is consistent with values obtained in summer for midlatitude sites without any influence of synoptic wind ([49,50]). This highlights that lower mistral winds favor the development of local circulations, as found in [43].

In winter, during the nighttime of 19 February to 20 February, when the mistral was established, the ABLH minimum was found to be higher in winter than what is usually found in the literature for continental sites [48,51]. In addition, the decrease in the ABLH was attenuated compared to other sites [49] because the high wind speed which characterizes mistral inhibits air mass cooling.

Moreover, the high wind speed can also explain the low growth rate observed on 19 February, compared to the literature for continental sites ([26,52,53]), where only heating processes drive the ABLH evolution, whereas in our coastal site, the ABLH growth rate comes from a combination of both heating and turbulence processes, this latter being predominant in mistral situations: the higher mechanical turbulence due to the mistral wind prevents the cooling of the nocturnal boundary layer and inhibits the development of the ABLH [17].

The diversity of the encountered mistral conditions yields a large variability in the ABLH seasonality. However, some features appear to be specific to such conditions.

The ABLH diurnal cycle is similar or greater in summer than in winter. In the literature, the difference of maximum between summer and winter in a typical midlatitude continental

site ranges from 800 m to 1000 m [52,54–57], whereas for mistral conditions in Marseille, we observed no such difference while the air masses came mainly from inland (around 330 m maximum).

The ABLH minimum inferred during the studied mistral events for both seasons was relatively high (400–585 m) compared to that found in the literature, where it stands between 100 m to 300 m [54,55] because of the high turbulence induced by such strong wind conditions. Turbulence, preventing the increase in the ABLH by heating [17], can also limit its decrease by cooling.

The ABLH diurnal amplitude in summer is higher than in winter, which is a very common result [54] because of more heating during summer than in winter.

3.4.2. Sea/Land Breezes

In summer, the sea breeze established around 2 h after sunrise, when the air above the continent became warmer than the air above the sea. Controversially, when the temperature of the ground fell below the temperature of the sea, the land breeze developed (between 19:00 and 22:00). The sea breeze lasted 12 to 14 h, which is the typical time range found in the literature for Mediterranean cities [58–60].

The sea breeze event described in this study shows a different ABLH diurnal cycle than the one found in most of the literature for coastal (except Marseille) sites [21,50,55], continental sites of sites [26,29,54,56], and during the ESCOMPTE campaign [24]. We previously supposed that it was due to the sea breeze head, as this maximum occurs at the same time as the sea/land breeze rotation. This result was also found by [19].

It has been proven [2,55,61] that the marine boundary layer is shallower than the continental boundary layer due to the sea's thermal inertia. This characteristic was also observable in our case study. The ABLH maximum during the sea breeze regime was lower than the one measured above continental sites during summer [26,48,52,54,56,57,62]. It was even lower than the ABLH maximum measured in other coastal cities during summer [50,63,64] because they are partly influenced by continental winds. However, we did not observe any pulsed sea breeze, as in [24]. One explanation could be that the sea breeze in our case was from the southwest (from 200° to 250°), contrary to ESCOMPTE which observed the pulsed sea breeze during a pure western sea breeze event.

The ABLH maximum during sea breeze was similar to that found during the ESCOMPTE campaign and consistent with the literature, which typically ranges from 400 to 800 m [65].

In the literature, the mean ABLH values at coastal sites include both the influence of marine and continental air masses. This can explain why the ABLH minimum that we infer during the studied sea breeze event was greater than both the ABLH mean values and the mean ABLH minimum, the latter below 600 m [50,54,56,63].

Anticyclonic conditions associated with sea/land breezes correspond to the regional stagnation of pollutants [66], which likely explains the existence of anthropogenic aerosols up to 4000 m. The lower layer from 100 m to 400 m, also associated with anthropogenic aerosols, can be associated with an urban layer, that is to say, aerosol emitted by the city.

Sea breeze, as the ABLH during such events, is poorly documented in the literature for the winter season, which makes our results unique.

In winter, the sea breeze duration agrees with those found in former studies for the Mediterranean area [59,60]. The sea breeze establishes 2 to 4 h after sunrise, which is around 07:00 in mid-December. It lasts between 6 and 7 h during the daytime, which is closer to what was observed in Alicante (mean duration time of 7 h, [59] or on the Levant coast of Spain [60]). The sea breeze ends with sunset, stopping 1 h or less after sunset time. For WB, our ABLH values were lower than midlatitude coastal site average ABLHs [26,55,63] due to the weaker influence of sea breezes at the latter.

During land breeze situations, the air temperature is very low (always below 7.0 °C), which triggers a very low ABLH that we estimate to be lower than 150 m, as it is not visible nor detected. Furthermore, due to the continental influence of the land breeze, our results

are comparable to other continental wintertime urban ABLH studies, which estimate the ABLH to be between 100 m and 300 m [67,68].

Our estimation of the ABLH diurnal amplitude is lower than that found in the literature for continental sites [56,69,70]. This can be explained by the fact that as the marine air masses arrive late on land, they start to heat up later in Marseille than in other continental sites. However, we lack comparative studies on the amplitude of the ABLH diurnal cycles during winter to make robust conclusions.

Comparing summer and winter, the ABLH maximum was higher in summer than in winter. However, this difference was relatively small compared to the one found between both seasons for continental (which is generally in the order of magnitude of 800 m to 1000 m [27,52,56]). This might be explained by the sea thermal inertia between both seasons.

4. Advantages and Limitations of Instruments and Methods

In this section, we discuss the limitations of both our instrumentation and the Haar method to infer the ABLH in Marseille.

4.1. Lidar Limitations

In this study, we reached the limitations of both lidar instruments. The manufacturer determined the blind zone altitude for the green channel as 100 m and 250 m for summer and winter, respectively, and 150 m for the near-infrared channel. Although this does not influence the ABLH analysis in summer, our study showed that in winter, particularly during sea/land breeze situations, the ABLH can be very thin, especially during the nighttime because of the relatively cold temperatures inhibiting the ABLH development. This limitation has also been found in other studies, such as that by [71]. To assess the ABLH values in the lidar blind zone, we recommend using a ceilometer. In fact, a ceilometer such as a Vaisala CL31 has been shown to have a blind zone of around 70 m [64,72]. Moreover, such ceilometer instrumentation has shown a good ability to detect the ABLH values up to 4 km altitude during the daytime [30], even if limited to 1–2 km by high solar noise, especially during summertime in the midlatitudes of the Northern Hemisphere, where more powerful lidar instruments are perfectly capable differentiating noise and backscattered signals. Combining lidar and ceilometer could be a good way to retrieve the ABLH and aerosol layers from around 70 m to 12 km altitude.

4.2. Haar Wavelet Method Limitations

The Haar wavelet method shows a good ability to detect the ABLH when the latter is defined by a clear aerosol gradient. This is efficient in cases of multiple layers when the aerosol gradient defining the ABLH is more pronounced than the layers above it. Finally, this method is able to differentiate layers from clouds and, therefore, will not wrongly choose a cloudy layer as the ABLH. However, the Haar wavelet method is limited in two situations: when there are too many layers and when there are no aerosol gradients because, in the latter, there is no exploitable signal delivered by either lidar or ceilometer.

During the SB event, we clearly see multiple layers above the ABLH, with gradients sometimes higher than those of the ABLH. As the purpose of the algorithm is to detect gradients, the Haar method may overestimate the ABLH by selecting the top of a higher layer [71]. The method we chose in this study was to select the altitude range in which the algorithm should search for the ABLH. By default, this range of altitudes was set from the altitude of the blind zone to 3000 m, based on typical values found for midlatitude sites. When an aerosol layer is incorrectly selected by the algorithm, we adapt the altitude range to exclude this aerosol layer. Otherwise, when the situation is too complicated, other algorithms more suitable for distinguishing layers of atmosphere should be investigated, as discussed below.

However, some new algorithms such as STRATfinder ([73]) consider both the gradient and the temporal continuity of the ABLH. To ensure this temporal continuity, the jump to

aerosol layers above the ABL would considerably decrease. The ability of this algorithm to retrieve the ABLH for both high and low signal-to-noise ratio instruments has already been demonstrated [74]. Another possibility would be to use machine learning [52,75]. In [75], the authors developed an algorithm based on this method to retrieve the ABLH in complex stratification and cloudy situations and compared it with other methods such as the Haar wavelet method. They showed that machine learning presented the best results of all the methods tested, which makes it promising.

4.3. Impact of the Choice of Dilation on the ABLH

As the ABLH determination relies on indirect lidar measurements, it is complicated to assess the associated uncertainties. Some studies have tackled this problem. For example, by comparing radio soundings and lidar measurements, Ref. [76] determined that the uncertainty of the Haar wavelet method used in that study was ± 60 m. This uncertainty includes the uncertainties of both the aerosol-based and the temperature-based methods, which can be large [77]. The uncertainties induced by the choice of parameters of the method have not been assessed so far.

Some studies have already shown that the choice of dilation is important in providing correct estimates of the ABLH. Using wavelet theory, [25] shows that a very low dilation, for example, a few tens of meters, may give too much importance to gradients induced by noise. These results have been confirmed by [32], whereas typical values of the used dilation were ranging from 60 m to 300 m [78], depending on instruments and sites. In the following, we quantify the error when choosing the dilation value. To do so, we calculate the sensibility S :

$$S = \frac{\frac{\Delta Y}{Y}}{\frac{\Delta X}{X}} \quad (4)$$

In our case, these yields:

$$S = \frac{\frac{\Delta ABLH}{ABLH}}{\frac{\Delta a}{a}} = \frac{\frac{ABLH_{ref} - ABLH}{ABLH_{ref}}}{\frac{a_{ref} - a}{a}} \quad (5)$$

The sensitivity of the ABLH to dilation is calculated for each event averaged over 10 min. The sensitivity gives the impact on the ABLH of a relative change in the dilation around the reference. For example, a change in the dilation of 3%, with a sensitivity of 2, leads to a change of 6% in the ABLH.

Then, the average of all the sensibilities over the time series per event is calculated and indicated in the 4th column of Table 5. The standard deviation for all sensitivity studies is also calculated (5th column of Table 5).

Table 5. Dilation sensitivity study for the four case studies.

Event	Dilation of Reference	Dilation for the Sensibility Study	Mean Sensibility (%/%)	Standard Deviation of Sensibility (%/%)
SM	270	240	0.09	1
WM	270	240	0.80	5
SB	240	210	0.10	10
WB	270	240	-0.20	1

For all cases, the sensitivity appears to be really low, which means that the choice of dilation does not greatly affect the calculated ABLH. However, the high standard deviation associated with each dilation implies that even if this choice does not impact most of the data points, some could be highly affected by this choice, detecting wrong layers instead of the ABLH.

4.4. Recommendations for Undetermined Situations

In some situations, the ABLH cannot be assessed visually because of a too complex situation (e.g., SB, with several aerosol layers up to 4000 m altitude) or when the aerosol gradient marking the entrainment zone is too weak (e.g., the end of the day on 16 August 2021). In this section, we suggest a few ways to overcome this indeterminacy.

Complementary instruments could be installed on the Longchamp site to determine the ABLH with greater accuracy. One way could be to install a wind ultra-high frequency (UHF) lidar, as in [17]. This instrument has already shown great results ([24]), especially in the case of sea/land breezes because it allows the boundary layer to be separated from the free atmosphere, as well as the internal patterns of the sea breeze current such as the sea breeze head or Kelvin–Helmholtz instabilities ([19]). It also provides complementary measurements, e.g., wind speeds and direction. This could be useful when coupled with aerosol lidar, as lidar measurement provides information on the aerosol layer, and wind UHF would provide information on the displacement of these layers. Using wind UHF and aerosol layers to determine the ABLH would result in two ABLH time series based on different definitions, and thus help reduce uncertainties.

Balloon launches could also be considered because the ABLH can be easily retrieved from potential temperature or wind speed profiles with different methods [2,27,79–81]. This would be particularly useful in cases of mistral wind. Indeed, as explained above, depending on the wind configuration and its speed, and due to the high mountains around the Rhône Valley, the flow could be affected by topographic features, such as hydraulic jump [46] or shelter effects [17]. These effects are diagnosable with the dimensionless Froude number, Fr , which requires the vertical gradient of potential temperature. Depending on if Fr is lower than, equal to, or greater than 1, assumptions can be made about the behavior of the wind compared with an obstacle. This was largely conducted in [17,82], obtaining interesting results. However, regarding the location of the Longchamp site, which is in the city center, legislation and authorization could be hard to come by. Moreover, they are very expensive in terms of human and material resources.

It should be noted that these methods are also complementary, thanks to the different information they provide. Studies have shown that, in some complex situations, lidar cannot be used alone [83], which is also confirmed by our study. To study ABLH, we suggest installing a ceilometer close to the lidar system, since the ceilometer has a very low blind zone [64,72]. Moreover, radio soundings launched far from Marseille in mistral flow, as in ESCOMPTE, could be useful for characterizing the air mass arriving above the city.

5. Conclusions

In this paper, we investigated the variability in two typical meteorological situations in the SUD–PACA region: mistral and sea/land breezes. These meteorological situations were compared in summer and winter to highlight seasonal differences. We set up a lidar in the city center during the summer of 2021 and in the winter of 2021–2022.

The mistral is a strong wind from the northwest, with wind speeds higher than 16 m/s in both summer and winter. Mistral situations can vary considerably depending on the curvature of the wind, its strength, and its constancy. The ABLH diurnal cycle is driven by the relative contribution of heat release from the land to the atmosphere due to incoming solar radiation and the turbulence associated with the high wind speed characteristics of the mistral. For well-established mistral, high mechanical turbulence limits the decrease in the ABLH at the end of the day, resulting in a relatively high ABLH during the nighttime; during the daytime, it inhibits the development of the ABLH by the heating process. The ABLH shows equal or higher values during summer than winter as mechanical turbulence induced by mistral winds does not depend on the season. When the mistral is too weak, the mechanical turbulence is no more a significant driving factor and the heating process mainly contributes to the development of the diurnal ABLH and its decrease at nighttime. To understand the ABLH variability during these mistral situations, it is thus important to

have an overview of the dynamics within a 500 km radius (including the Rhône Valley) and to not only focus on one specific site.

Sea breeze events are characterized by relatively calm conditions during the daytime, with wind speeds between 4 and 6 m/s coming from the sea with a southwest wind direction. Sea breezes last longer during summer than during winter due to more intense land ground heating, incoming solar radiation, and longer day length. Land breezes occur during the nighttime with north-east wind directions associated with relatively low wind speeds (below 3 m/s). Land breezes last longer during winter due to the cold atmospheric temperature associated with high sea inertia, resulting in a higher temperature at the sea surface than at the continental (15.0°C). The ABLH diurnal cycle is marked by a higher maximum, minimum, and growth rate of the ABLH in summer than in winter. Since the Mediterranean Sea has greater thermal inertia and lower roughness than the land, the ABLH of air masses coming from the sea has smaller variability than the ABLH of continental air masses. The ABLH is less than 150 m in winter; however, it could not be detected more precisely due to the blind zone of the lidar. The stratification of the aerosol layers in sea/land breeze situations is more developed in summer, with aerosol layers up to 4000 m, likely due to both stagnant conditions and sea breeze cells. A deeper investigation of the dynamics with a high-resolution 3D model would be useful to fully understand the atmospheric dynamics in such cases.

Due to instrumental limitations, the near-infrared channel could provide ABLH estimates starting from 150 m, contrary to the green channel, which is blind below 250 m. The near-infrared channel, therefore, has a better performance than the green channel when it comes to detecting the ABLH. However, the lidar does not separate polarized and depolarized signals from the near-infrared channel and, thus, it is not able to characterize the type of aerosols to provide information about the origin of air masses.

The results of this study allow us to draw some conclusions and propose the following suggestions to improve the coverage of the ABLH measurements in a coastal city such as Marseille:

- The ABLH retrieval calculations need to be carefully assessed. In cases when the Haar method is chosen, there is no overall difference whatever the chosen dilation. However, dense aerosol layers on top of the ABL and/or a weak aerosol gradient between the atmospheric boundary layer and the free atmosphere could limit the detection of the ABLH by algorithms.
- The blind zone associated with lidar instruments is a limitation in cases of an ABLH lower than the blind zone (e.g., winter nighttime ABLH); therefore, using a complementary instrument that can detect low ABLH, such as a ceilometer, is suggested.
- A combination of green and near-infrared channels, as performed in this study, is found to be helpful when improving the detection and study of the ABLH.
- Enhancing the lidar performance to separate the parallel and perpendicular components of the near-infrared signal would be of benefit.
- Lidar measurements alone are limited when used to determine the ABLH in complex cases; for example, when there are multiple aerosol layers in the lower part of the atmosphere. Therefore, 3D models and/or complementary measurements, such as thermodynamic variables, are necessary to understand the atmospheric dynamics of the region of study.

Finally, this work only focused on one case for both of the studied meteorological situations and two seasons. To allow the generalization of these results, more cases should be studied across all four seasons, especially since it has been proven that mistral and sea/land breezes could have very specific patterns depending on atmospheric dynamics. This study adds to the few previous studies on ABLH variability in the Mediterranean basin. However, it is the first to measure the ABLH in winter in Marseille, to assess the seasonality of the ABLH, and to provide the ABLH during both the day and nighttime in summer in this Mediterranean coastal city.

Author Contributions: Conceptualization, I.X.-R.; methodology, A.R., I.X.-R., I.P. and P.G.; software, A.R. and I.P.; validation, I.X.-R., I.P. and P.G.; formal analysis, A.R., I.X.-R. and L.L.; investigation, A.R. and I.X.-R.; resources, A.A., I.P., P.G. and I.X.-R.; writing—original draft preparation, A.R.; writing—review and editing, all of the authors; supervision, I.X.-R.; project administration, I.X.-R.; funding acquisition, I.X.-R. All authors have read and agreed to the published version of the manuscript.

Funding: The French National Research Agency (ANR), grant number ANR-19-CE03-0008 funded the research and the PhD grant of A. Riandet within the ANR COOL-AMmetropolis project and the lidar instrumentation in the winter of 2021–2022.

Data Availability Statement: Our datasets are available upon request to the instrument PI, I. Xueref-Remy (irene.remy-xueref@univ-amu.fr). They will be made openly accessible at the end of the ANR COOL-AMm project in 2025, following the project consortium agreement.

Acknowledgments: We deeply thank the regional air quality monitoring ATMOSUD and especially Grégory Gille for allowing us to set up our lidar instrumentation at the Marseille–Longchamp station. We are grateful to the CIMEL company for lending us lidar equipment during the summer of 2021 while waiting for our lidar instrument to be set up. We thank the Infoclimat association and Laurent Garcelon for providing us with meteorological data. We also acknowledge the Service National d’Observation (SNO PHOTONS), which manages aerosol remote sensing instrumentation in France within the framework of ACTRIS-France and especially Thierry Podvin for lending us the photometer instrument.

Conflicts of Interest: The authors declare no conflict of interest.

References

1. Stull, R.B. *An Introduction to Boundary Layer Meteorology*; Springer Science & Business Media: Berlin/Heidelberg, Germany, 1988.
2. Gu, J.; Zhang, Y.; Yang, N.; Wang, R. Diurnal Variability of the Planetary Boundary Layer Height Estimated from Radiosonde Data. *Earth Planet. Phys.* **2020**, *4*, 479–492. [[CrossRef](#)]
3. Wang, M.; Tang, G.; Liu, Y.; Ma, M.; Yu, M.; Hu, B.; Zhang, Y.; Wang, Y.; Wang, Y. The Difference in the Boundary Layer Height between Urban and Suburban Areas in Beijing and Its Implications for Air Pollution. *Atmos. Environ.* **2021**, *260*, 118552. [[CrossRef](#)]
4. Brahmanandam, P.S.; Kumar, V.N.; Kumar, G.A.; Rao, M.P.; Samatha, K.; Ram, S.T. A Few Important Features of Global Atmospheric Boundary Layer Heights Estimated Using COSMIC Radio Occultation Retrieved Data. *Indian J. Phys.* **2020**, *94*, 555–563. [[CrossRef](#)]
5. Alexiou, D.; Kokkalis, P.; Papayannis, A.; Rocadenbosch, F.; Argyrouli, A.; Tsaknakis, G.; Tzanis, C.G. Planetary Boundary Layer Height Variability over Athens, Greece, Based on the Synergy of Raman Lidar and Radiosonde Data: Application of the Kalman Filter and Other Techniques (2011–2016). *EPJ Web Conf.* **2018**, *176*, 06007. [[CrossRef](#)]
6. Sicard, M.; Perez, C.; Comeren, A.; Baldasano, J.M.; Rocadenbosch, F. Determination of the Mixing Layer Height from Regular Lidar Measurements in the Barcelona Area. In *Remote Sensing of Clouds and the Atmosphere VIII*; SPIE: Barcelona, Spain, 2004; Volume 5235, pp. 505–516.
7. Pandolfi, M.; Martucci, G.; Querol, X.; Alastuey, A.; Wilsenack, F.; Frey, S.; O'Dowd, C.D.; Dall'Osto, M. Continuous Atmospheric Boundary Layer Observations in the Coastal Urban Area of Barcelona during SAPUSS. *Atmos. Chem. Phys.* **2013**, *13*, 4983–4996. [[CrossRef](#)]
8. Peña, A.; Gryning, S.-E.; Hahmann, A.N. Observations of the Atmospheric Boundary Layer Height under Marine Upstream Flow Conditions at a Coastal Site: COASTAL BOUNDARY LAYER HEIGHT. *J. Geophys. Res. Atmos.* **2013**, *118*, 1924–1940. [[CrossRef](#)]
9. Lelandais, L.; Xueref-Remy, I.; Riandet, A.; Blanc, P.E.; Armengaud, A.; Oppo, S.; Yohia, C.; Ramonet, M.; Delmotte, M. Analysis of 5.5 Years of Atmospheric CO₂, CH₄, CO Continuous Observations (2014–2020) and Their Correlations, at the Observatoire de Haute Provence, a Station of the ICOS-France National Greenhouse Gases Observation Network. *Atmos. Environ.* **2022**, *277*, 119020. [[CrossRef](#)]
10. Marley, H.G.; Dirks, K.N.; Neverman, A.J.; McKendry, I.; Salmond, J.A. The Relationship between Brown Haze, Atmospheric Boundary Layer Structure, and Air Pollution in an Urban Area of Complex Coastal Terrain. *Atmos. Pollut. Res.* **2021**, *12*, 101057. [[CrossRef](#)]
11. Banks, R.F.; Baldasano, J.M. Impact of WRF Model PBL Schemes on Air Quality Simulations over Catalonia, Spain. *Sci. Total Environ.* **2016**, *572*, 98–113. [[CrossRef](#)]
12. Kotthaus, S.; Bravo-Aranda, J.A.; Collaud Coen, M.; Guerrero-Rascado, J.L.; Costa, M.J.; Cimini, D.; O'Connor, E.J.; Hervo, M.; Alados-Arboledas, L.; Jiménez-Portaz, M.; et al. Atmospheric Boundary Layer Height from Ground-Based Remote Sensing: A Review of Capabilities and Limitations. *Atmos. Meas. Tech.* **2022**, *16*, 433–479. [[CrossRef](#)]
13. Li, D.; Wu, Y.; Gross, B.; Moshary, F. Capabilities of an Automatic Lidar Ceilometer to Retrieve Aerosol Characteristics within the Planetary Boundary Layer. *Remote Sens.* **2021**, *13*, 3626. [[CrossRef](#)]
14. Dang, R.; Yang, Y.; Li, H.; Hu, X.-M.; Wang, Z.; Huang, Z.; Zhou, T.; Zhang, T. Atmosphere Boundary Layer Height (ABLH) Determination under Multiple-Layer Conditions Using Micro-Pulse Lidar. *Remote Sens.* **2019**, *11*, 263. [[CrossRef](#)]

15. Cros, B.; Durand, P.; Cachier, H.; Drobinski, P.; Fréjafon, E.; Kottmeier, C.; Perros, P.E.; Peuch, V.-H.; Ponche, J.-L.; Robin, D.; et al. The ESCOMPTE Program: An Overview. *Atmos. Res.* **2004**, *69*, 241–279. [[CrossRef](#)]
16. Corsmeier, U.; Behrendt, R.; Drobinski, P.; Kottmeier, C. The Mistral and Its Effect on Air Pollution Transport and Vertical Mixing. *Atmos. Res.* **2005**, *74*, 275–302. [[CrossRef](#)]
17. Drobinski, P.; Bastin, S.; Guenard, V.; Caccia, J.-L.; Dabas, A.M.; Delville, P.; Protat, A.; Reitebuch, O.; Werner, C. Summer Mistral at the Exit of the Rhône Valley. *Q. J. R. Meteorol. Soc.* **2005**, *131*, 353–375. [[CrossRef](#)]
18. Pettre, P. On the Problem of Violent Valley Winds. *J. Atmos. Sci.* **1982**, *39*, 542–554. [[CrossRef](#)]
19. Miller, S.T.K.; Keim, B.D.; Talbot, R.W.; Mao, H. Sea Breeze: Structure, Forecasting, and Impacts. *Rev. Geophys.* **2003**, *41*, 1–31. [[CrossRef](#)]
20. Bastin, S.; Drobinski, P. Sea-Breeze-Induced Mass Transport over Complex Terrain in South-Eastern France: A Case-Study. *Q. J. R. Meteorol. Soc.* **2006**, *132*, 405–423. [[CrossRef](#)]
21. Augustin, P.; Delbarre, H.; Lohou, F.; Campistron, B.; Puygrenier, V.; Cachier, H.; Lombardo, T. Investigation of Local Meteorological Events and Their Relationship with Ozone and Aerosols during an ESCOMPTE Photochemical Episode. *Ann. Geophys.* **2006**, *24*, 2809–2822. [[CrossRef](#)]
22. Mestayer, P.G.; Durand, P.; Augustin, P.; Bastin, S.; Bonnefond, J.-M.; Bénech, B.; Campistron, B.; Coppalle, A.; Delbarre, H.; Dousset, B.; et al. The Urban Boundary-Layer Field Campaign in Marseille (Ubl/Clu-Escompte): Set-up and First Results. *Bound.-Layer Meteorol.* **2005**, *114*, 315–365. [[CrossRef](#)]
23. Lee, Y.-H.; Park, M.-S.; Choi, Y. Planetary Boundary-Layer Structure at an Inland Urban Site under Sea Breeze Penetration. *Asia-Pac. J. Atmos. Sci.* **2021**, *57*, 701–715. [[CrossRef](#)]
24. Puygrenier, V.; Lohou, F.; Campistron, B.; Saïd, F.; Pigeon, G.; Bénech, B.; Serça, D. Investigation on the Fine Structure of Sea-Breeze during ESCOMPTE Experiment. *Atmos. Res.* **2005**, *74*, 329–353. [[CrossRef](#)]
25. Brooks, I.M. Finding Boundary Layer Top: Application of a Wavelet Covariance Transform to Lidar Backscatter Profiles. *J. Atmos. Ocean. Technol.* **2003**, *20*, 1092–1105. [[CrossRef](#)]
26. Baars, H.; Ansmann, A.; Engelmann, R.; Althausen, D. Continuous Monitoring of the Boundary-Layer Top with Lidar. *Atmos. Chem. Phys.* **2008**, *8*, 7281–7296. [[CrossRef](#)]
27. Koffi, E.N.; Bergamaschi, P.; Karstens, U.; Krol, M.; Segers, A.; Schmidt, M.; Levin, I.; Vermeulen, A.T.; Fisher, R.E.; Kazan, V.; et al. Evaluation of the Boundary Layer Dynamics of the TM5 Model over Europe. *Geosci. Model Dev.* **2016**, *9*, 3137–3160. [[CrossRef](#)]
28. Toledo, D.; Córdoba-Jabonero, C.; Adame, J.A.; De La Morena, B.; Gil-Ojeda, M. Estimation of the Atmospheric Boundary Layer Height during Different Atmospheric Conditions: A Comparison on Reliability of Several Methods Applied to Lidar Measurements. *Int. J. Remote Sens.* **2017**, *38*, 3203–3218. [[CrossRef](#)]
29. Wang, D.; Stachlewska, I.S.; Song, X.; Heese, B.; Nemuc, A. Variability of the Boundary Layer Over an Urban Continental Site Based on 10 Years of Active Remote Sensing Observations in Warsaw. *Remote Sens.* **2020**, *12*, 340. [[CrossRef](#)]
30. Caicedo, V.; Rappenglück, B.; Lefer, B.; Morris, G.; Toledo, D.; Delgado, R. Comparison of Aerosol Lidar Retrieval Methods for Boundary Layer Height Detection Using Ceilometer Aerosol Backscatter Data. *Atmos. Meas. Tech.* **2017**, *10*, 1609–1622. [[CrossRef](#)]
31. Davis, K.J.; Gamage, N.; Hagelberg, C.R.; Kiemle, C. An Objective Method for Deriving Atmospheric Structure from Airborne Lidar Observations. *J. Atmos. Ocean. Technol.* **2000**, *17*, 1455–1468. [[CrossRef](#)]
32. Mortier, A. Tendances et Variabilités de l'aérosol Atmosphérique à l'aide Du Couplage Lidar/Photomètre Sur Les Sites de Lille et Dakar. Ph.D. Thesis, Lille 1, Villeneuve-d'Ascq, France, 2013.
33. Compton, J.C.; Delgado, R.; Berkoff, T.A.; Hoff, R.M. Determination of Planetary Boundary Layer Height on Short Spatial and Temporal Scales: A Demonstration of the Covariance Wavelet Transform in Ground-Based Wind Profiler and Lidar Measurements. *J. Atmos. Ocean. Technol.* **2013**, *30*, 1566–1575. [[CrossRef](#)]
34. Bohlmann, S.; Baars, H.; Radenz, M.; Engelmann, R.; Macke, A. Ship-Borne Aerosol Profiling with Lidar over the Atlantic Ocean: From Pure Marine Conditions to Complex Dust-Smoke Mixtures. *Atmos. Chem. Phys.* **2018**, *18*, 9661–9679. [[CrossRef](#)]
35. Groß, S.; Esselborn, M.; Weinzierl, B.; Wirth, M.; Fix, A.; Petzold, A. Aerosol Classification by Airborne High Spectral Resolution Lidar Observations. *ACP* **2013**, *13*, 2487–2505. [[CrossRef](#)]
36. Xie, C.; Nishizawa, T.; Sugimoto, N.; Matsui, I.; Wang, Z. Characteristics of Aerosol Optical Properties in Pollution and Asian Dust Episodes over Beijing, China. *Appl. Opt.* **2008**, *47*, 4945. [[CrossRef](#)]
37. Freudenthaler, V.; Esselborn, M.; Wiegner, M.; Heese, B.; Tesche, M.; Ansmann, A.; MüLLER, D.; Althausen, D.; Wirth, M.; Fix, A.; et al. Depolarization Ratio Profiling at Several Wavelengths in Pure Saharan Dust during SAMUM 2006. *Tellus B Chem. Phys. Meteorol.* **2009**, *61*, 165–179. [[CrossRef](#)]
38. Rupakheti, D.; Kang, S.; Rupakheti, M.; Cong, Z.; Tripathee, L.; Panday, A.K.; Holben, B.N. Observation of Optical Properties and Sources of Aerosols at Buddha's Birthplace, Lumbini, Nepal: Environmental Implications. *Environ. Sci. Pollut. Res.* **2018**, *25*, 14868–14881. [[CrossRef](#)] [[PubMed](#)]
39. Groß, S.; Tesche, M.; Freudenthaler, V.; Toledano, C.; Wiegner, M.; Ansmann, A.; Althausen, D.; Seefeldner, M. Characterization of Saharan Dust, Marine Aerosols and Mixtures of Biomass-Burning Aerosols and Dust by Means of Multi-Wavelength Depolarization and Raman Lidar Measurements during SAMUM 2. *Tellus B Chem. Phys. Meteorol.* **2011**, *63*, 706–724. [[CrossRef](#)]
40. Holben, B.N.; Eck, T.F.; Slutsker, I.; Tanré, D.; Buis, J.P.; Setzer, A.; Vermote, E.; Reagan, J.A.; Kaufman, Y.J.; Nakajima, T.; et al. AERONET—A Federated Instrument Network and Data Archive for Aerosol Characterization. *Remote Sens. Environ.* **1998**, *66*, 1–16. [[CrossRef](#)]

41. Lemonsu, A.; Grimmond, C.S.B.; Masson, V. Modeling the Surface Energy Balance of the Core of an Old Mediterranean City: Marseille. *J. Appl. Meteorol.* **2004**, *43*, 312–327. [[CrossRef](#)]
42. Lemonsu, A.; Bastin, S.; Masson, V.; Drobinski, P. Vertical Structure of the Urban Boundary Layer over Marseille Under Sea-Breeze Conditions. *Bound.-Layer Meteorol.* **2006**, *118*, 477–501. [[CrossRef](#)]
43. Bastin, S.; Drobinski, P.; Guénard, V.; Caccia, J.-L.; Campistron, B.; Dabas, A.M.; Delville, P.; Reitebuch, O.; Werner, C. On the Interaction between Sea Breeze and Summer Mistral at the Exit of the Rhône Valley. *Mon. Weather Rev.* **2006**, *134*, 1647–1668. [[CrossRef](#)]
44. Groß, S.; Freudenthaler, V.; Wirth, M.; Weinzierl, B. Towards an Aerosol Classification Scheme for Future EarthCARE Lidar Observations and Implications for Research Needs. *Atmos. Sci. Lett.* **2015**, *16*, 77–82. [[CrossRef](#)]
45. Mylonaki, M.; Giannakaki, E.; Papayannis, A.; Papanikolaou, C.-A.; Komppula, M.; Nicolae, D.; Papagiannopoulos, N.; Amodeo, A.; Baars, H.; Soupiona, O. Aerosol Type Classification Analysis Using EARLINET Multiwavelength and Depolarization Lidar Observations. *Atmos. Chem. Phys.* **2021**, *21*, 2211–2227. [[CrossRef](#)]
46. Guenard, V.; Drobinski, P.; Caccia, J.-L.; Campistron, B.; Bench, B. An Observational Study of the Mesoscale Mistral Dynamics. *Bound.-Layer Meteorol.* **2005**, *115*, 263–288. [[CrossRef](#)]
47. Jiang, Q.; Smith, R.B.; Doyle, J. The Nature of the Mistral: Observations and Modelling of Two MAP Events. *Q. J. R. Meteorol. Soc.* **2003**, *129*, 857–875. [[CrossRef](#)]
48. Menut, L.; Flamant, C.; Pelon, J.; Flamant, P.H. Urban Boundary-Layer Height Determination from Lidar Measurements over the Paris Area. *Appl. Opt.* **1999**, *38*, 945. [[CrossRef](#)] [[PubMed](#)]
49. Barlow, J.F.; Dunbar, T.M.; Nemitz, E.G.; Wood, C.R.; Gallagher, M.W.; Davies, F.; O'Connor, E.; Harrison, R.M. Boundary Layer Dynamics over London, UK, as Observed Using Doppler Lidar during REPARTEE-II. *Atmos. Chem. Phys.* **2011**, *11*, 2111–2125. [[CrossRef](#)]
50. Kotthaus, S.; Grimmond, C.S.B. Atmospheric Boundary-layer Characteristics from Ceilometer Measurements. Part 2: Application to London's Urban Boundary Layer. *Q. J. R. Meteorol. Soc.* **2018**, *144*, 1511–1524. [[CrossRef](#)]
51. Wang, L.; Fan, S.; Miao, S.; Yang, A.; Li, Y.; Liu, J.; Liu, C.; Chen, S.; Ho, H.C.; Gao, Z.; et al. Vertical Gradient Variations in Radiation Budget and Heat Fluxes in the Urban Boundary Layer: A Comparison Study between Polluted and Clean Air Episodes in Beijing during Winter. *Atmospheres* **2020**, *12*, e2020JD032478. [[CrossRef](#)]
52. De Arruda Moreira, G.; Guerrero-Rascado, J.L.; Bravo-Aranda, J.A.; Foyo-Moreno, I.; Cazorla, A.; Alados, I.; Lyamani, H.; Landulfo, E.; Alados-Arboledas, L. Study of the Planetary Boundary Layer Height in an Urban Environment Using a Combination of Microwave Radiometer and Ceilometer. *Atmos. Res.* **2020**, *240*, 104932. [[CrossRef](#)]
53. Pichelli, E.; Ferretti, R.; Cacciani, M.; Siani, A.M.; Ciardini, V.; Di Iorio, T. The Role of Urban Boundary Layer Investigated with High-Resolution Models and Ground-Based Observations in Rome Area: A Step towards Understanding Parameterization Potentialities. *Atmos. Meas. Tech.* **2014**, *7*, 315–332. [[CrossRef](#)]
54. Pal, S.; Haefelin, M. Forcing Mechanisms Governing Diurnal, Seasonal, and Interannual Variability in the Boundary Layer Depths: Five Years of Continuous Lidar Observations over a Suburban Site near Paris. *J. Geophys. Res. Atmos.* **2015**, *120*, 11936–11956. [[CrossRef](#)]
55. De Tomasi, F.; Miglietta, M.M.; Perrone, M.R. The Growth of the Planetary Boundary Layer at a Coastal Site: A Case Study. *Bound.-Layer Meteorol.* **2011**, *139*, 521–541. [[CrossRef](#)]
56. Lotteraner, C.; Piringer, M. Mixing-Height Time Series from Operational Ceilometer Aerosol-Layer Heights. *Bound.-Layer Meteorol.* **2016**, *161*, 265–287. [[CrossRef](#)]
57. Granados-Muñoz, M.J.; Navas-Guzmán, F.; Bravo-Aranda, J.A.; Guerrero-Rascado, J.L.; Lyamani, H.; Fernández-Gálvez, J.; Alados-Arboledas, L. Automatic Determination of the Planetary Boundary Layer Height Using Lidar: One-Year Analysis over Southeastern Spain: DETERMINATION OF THE PBL HEIGHT. *J. Geophys. Res. Atmos.* **2012**, *117*, D18208. [[CrossRef](#)]
58. Savov, P.; Kolev, N.; Kolarova, M.; Batchvarova, E.; Barantiev, D. *Aerosols, Ozone and CO₂ under Sea-Breeze Conditions at a Black Sea Coastal Site*; AIP Publishing LLC: Sofia, Bulgaria, 2019; p. 120003.
59. Azorin-Molina, C.; Chen, D.; Tijm, S.; Baldi, M. A Multi-Year Study of Sea Breezes in a Mediterranean Coastal Site: Alicante (Spain): Multi-Year Study of Sea Breezes in a Mediterranean Coastal Site. *Int. J. Climatol.* **2011**, *31*, 468–486. [[CrossRef](#)]
60. Cantos, J.O.; Molina, C.A. The Meteorological Importance of Sea-Breezes in the Levant Region of Spain: The Meteorological Importance of Sea-Breezes in the Levant Region of Spain. *Weather* **2004**, *59*, 282–286. [[CrossRef](#)]
61. Shang, F.; Chen, D.; Guo, X.; Lang, J.; Zhou, Y.; Li, Y.; Fu, X. Impact of Sea Breeze Circulation on the Transport of Ship Emissions in Tangshan Port, China. *Atmosphere* **2019**, *10*, 723. [[CrossRef](#)]
62. Manninen, A.J.; Marke, T.; Tuononen, M.; O'Connor, E.J. Atmospheric Boundary Layer Classification With Doppler Lidar. *J. Geophys. Res. Atmos.* **2018**, *123*, 8172–8189. [[CrossRef](#)]
63. Haman, C.L.; Lefer, B.; Morris, G.A. Seasonal Variability in the Diurnal Evolution of the Boundary Layer in a Near-Coastal Urban Environment. *J. Atmos. Ocean. Technol.* **2012**, *29*, 697–710. [[CrossRef](#)]
64. Tsaknakis, G.; Papayannis, A.; Kokkalis, P.; Amiridis, V.; Kambezidis, H.D.; Mamouri, R.E.; Georgouassis, G.; Avdikos, G. Inter-Comparison of Lidar and Ceilometer Retrievals for Aerosol and Planetary Boundary Layer Profiling over Athens, Greece. *Atmos. Meas. Tech.* **2011**, *4*, 1261–1273. [[CrossRef](#)]
65. Melas, D.; Lavagnini, A.; Sempreviva, A.-M. An Investigation of the Boundary Layer Dynamics of Sardinia Island under Sea-Breeze Conditions. *J. Appl. Meteorol.* **2000**, *39*, 516–524. [[CrossRef](#)]

66. Augustin, P.; Billet, S.; Crumeyrolle, S.; Deboudt, K.; Dieudonné, E.; Flament, P.; Fourmentin, M.; Guilbaud, S.; Hanoune, B.; Landkocz, Y.; et al. Impact of Sea Breeze Dynamics on Atmospheric Pollutants and Their Toxicity in Industrial and Urban Coastal Environments. *Remote Sens.* **2020**, *12*, 648. [CrossRef]
67. Zhang, D.; Comstock, J.; Morris, V. Comparisons of Planetary Boundary Layer Height from Ceilometer with ARM Radiosonde Data. *Atmos. Meas. Tech.* **2022**, *15*, 4735–4749. [CrossRef]
68. Halios, C.H.; Barlow, J.F. Observations of the Morning Development of the Urban Boundary Layer Over London, UK, Taken During the ACTUAL Project. *Bound.-Layer Meteorol.* **2018**, *166*, 395–422. [CrossRef] [PubMed]
69. Rotach, M.W.; Vogt, R.; Bernhofer, C.; Batchvarova, E.; Christen, A.; Clappier, A.; Feddersen, B.; Gryning, S.-E.; Martucci, G.; Mayer, H.; et al. BUBBLE—An Urban Boundary Layer Meteorology Project. *Theor. Appl. Climatol.* **2005**, *81*, 231–261. [CrossRef]
70. Pal, S.; Xueref-Remy, I.; Ammoura, L.; Chazette, P.; Gibert, F.; Royer, P.; Dieudonné, E.; Dupont, J.-C.; Haeffelin, M.; Lac, C.; et al. Spatio-Temporal Variability of the Atmospheric Boundary Layer Depth over the Paris Agglomeration: An Assessment of the Impact of the Urban Heat Island Intensity. *Atmos. Environ.* **2012**, *63*, 261–275. [CrossRef]
71. Haeffelin, M.; Angelini, F.; Morille, Y.; Martucci, G.; Frey, S.; Gobbi, G.P.; Lolli, S.; O'Dowd, C.D.; Sauvage, L.; Xueref-Rémy, I.; et al. Evaluation of Mixing-Height Retrievals from Automatic Profiling Lidars and Ceilometers in View of Future Integrated Networks in Europe. *Bound.-Layer Meteorol.* **2012**, *143*, 49–75. [CrossRef]
72. Martucci, G.; Matthey, R.; Mitev, V.; Richner, H. Comparison between Backscatter Lidar and Radiosonde Measurements of the Diurnal and Nocturnal Stratification in the Lower Troposphere. *J. Atmos. Ocean. Technol.* **2007**, *24*, 1231–1244. [CrossRef]
73. Kotthaus, S.; Haeffelin, M.; Drouin, M.-A.; Dupont, J.-C.; Grimmond, S.; Haefele, A.; Hervo, M.; Poltera, Y.; Wiegner, M. Tailored Algorithms for the Detection of the Atmospheric Boundary Layer Height from Common Automatic Lidars and Ceilometers (ALC). *Remote Sens.* **2020**, *12*, 3259. [CrossRef]
74. Danchovski, V. Summertime Urban Mixing Layer Height over Sofia, Bulgaria. *Atmosphere* **2019**, *10*, 36. [CrossRef]
75. Liu, Z.; Chang, J.; Li, H.; Chen, S.; Dai, T. Estimating Boundary Layer Height from LiDAR Data under Complex Atmospheric Conditions Using Machine Learning. *Remote Sens.* **2022**, *14*, 418. [CrossRef]
76. Pal, S.; Haeffelin, M.; Batchvarova, E. Exploring a Geophysical Process-Based Attribution Technique for the Determination of the Atmospheric Boundary Layer Depth Using Aerosol Lidar and near-Surface Meteorological Measurements: New Attribution Lidar-derived ABL Depth. *J. Geophys. Res. Atmos.* **2013**, *118*, 9277–9295. [CrossRef]
77. Hennemuth, B.; Lammert, A. Determination of the Atmospheric Boundary Layer Height from Radiosonde and Lidar Backscatter. *Bound. -Layer Meteorol.* **2006**, *120*, 181–200. [CrossRef]
78. Mao, F.; Gong, W.; Song, S.; Zhu, Z. Determination of the Boundary Layer Top from Lidar Backscatter Profiles Using a Haar Wavelet Method over Wuhan, China. *Opt. Laser Technol.* **2013**, *49*, 343–349. [CrossRef]
79. Luo, T.; Yuan, R.; Wang, Z. Lidar-Based Remote Sensing of Atmospheric Boundary Layer Height over Land and Ocean. *Atmos. Meas. Tech.* **2014**, *7*, 173–182. [CrossRef]
80. Sivaraman, C.; McFarlane, S.; Chapman, E.; Jesen, M.; Toto, T.; Liu, S.; Fischer, M. Planetary Boundary Layer (PBL) Height Value Added Product (VAP): Radiosonde Retrievals. 2013. Available online: <https://www.osti.gov/biblio/1808688> (accessed on 20 February 2023).
81. Seidel, D.J.; Ao, C.O.; Li, K. Estimating Climatological Planetary Boundary Layer Heights from Radiosonde Observations: Comparison of Methods and Uncertainty Analysis. *J. Geophys. Res.* **2010**, *115*, D16113. [CrossRef]
82. Moppert, C.; Saïd, F.; Augustin, P.; Geffroy, S.; Delbarre, H.; Freville, P.; Fievert, A.; Campistron, B.; Frejafon, E. Urban Atmospheric Stratification and Its Dynamics: ABL Development above the City of Marseille and in the Surroundings. In Proceedings of the International Conference on Urban Air QUality Measurement Modelling and Management, Prague, Czech Republic, 25–27 March 2003.
83. Delbarre, H.; Augustin, P.; Saïd, F.; Campistron, B.; Bénech, B.; Lohou, F.; Puygrenier, V.; Moppert, C.; Cousin, F.; Fréville, P.; et al. Ground-Based Remote Sensing Observation of the Complex Behaviour of the Marseille Boundary Layer during ESCOMPTE. *Atmos. Res.* **2005**, *74*, 403–433. [CrossRef]

Disclaimer/Publisher's Note: The statements, opinions and data contained in all publications are solely those of the individual author(s) and contributor(s) and not of MDPI and/or the editor(s). MDPI and/or the editor(s) disclaim responsibility for any injury to people or property resulting from any ideas, methods, instructions or products referred to in the content.